

# Characterizing the Youngest Herschel-detected Protostars II. Molecular Outflows from the Millimeter and the Far-infrared<sup>1</sup>

John J. Tobin<sup>2,3</sup>, Amelia M. Stutz<sup>4</sup>, P. Manoj<sup>5</sup>, S. Thomas Megeath<sup>6</sup>, Agata Karska<sup>7</sup>,  
Zsolia Nagy<sup>6</sup>, Friedrich Wyrowski<sup>8</sup>, William Fischer<sup>6,9</sup>, Dan M. Watson<sup>10</sup>, Thomas Stanke<sup>11</sup>

## ABSTRACT

We present CARMA CO ( $J = 1 \rightarrow 0$ ) observations and *Herschel* PACS spectroscopy, characterizing the outflow properties toward extremely young and deeply embedded protostars in the Orion molecular clouds. The sample comprises a subset of the Orion protostars known as the PACS Bright Red Sources (PBRs) (Stutz et al.). We observed 14 PBRs with CARMA and 8 of these 14 with *Herschel*, acquiring full spectral scans from 55  $\mu\text{m}$  to 200  $\mu\text{m}$ . Outflows are detected in CO ( $J = 1 \rightarrow 0$ ) from 8 of 14 PBRs, with two additional tentative detections; outflows are also detected from the outbursting protostar HOPS 223 (V2775 Ori) and the Class I protostar HOPS 68. The outflows have a range of morphologies, some are spatially compact, <10000 AU in extent, while others extend beyond the primary beam. The outflow velocities and morphologies are consistent with

---

<sup>1</sup>*Herschel* is an ESA space observatory with science instruments provided by European-led Principal Investigator consortia and with important participation from NASA.

<sup>2</sup>Veni Fellow, Leiden Observatory, Leiden University, P.O. Box 9513, 2300-RA Leiden, The Netherlands; tobins@strw.leidenuniv.nl

<sup>3</sup>National Radio Astronomy Observatory, Charlottesville, VA 22903, USA

<sup>4</sup>Max-Planck-Institut für Astronomie, D-69117 Heidelberg, Germany

<sup>5</sup>Department of Astronomy and Astrophysics, Tata Institute of Fundamental Research, Colaba, Mumbai 400005, India

<sup>6</sup>Ritter Astrophysical Research Center, Department of Physics and Astronomy, University of Toledo, Toledo, OH 43560

<sup>7</sup>Centre for Astronomy, Nicolaus Copernicus University, Faculty of Physics, Astronomy and Informatics, Grudziadzka 5, PL-87100 Torun, Poland

<sup>8</sup>Max-Planck-Institut für Radioastronomie, Auf dem Hügel 69, 53121, Bonn, Germany

<sup>9</sup>NASA Goddard Space Flight Center, 8800 Greenbelt Road, Greenbelt, MD 20771

<sup>10</sup>Department of Physics and Astronomy, University of Rochester, Rochester, NY 14627

<sup>11</sup>European Southern Observatory, 85748 Garching bei München, Germany

being dominated by intermediate inclination angles ( $80^\circ \geq i \geq 20^\circ$ ). This confirms the interpretation of the very red  $24 \mu\text{m}$  to  $70 \mu\text{m}$  colors of the PBRS as a signpost of high envelope densities, with only one (possibly two) cases of the red colors resulting from edge-on inclinations. We detect high-J ( $J_{up} > 13$ ) CO lines and/or H<sub>2</sub>O lines from 5 of 8 PBRS and only for those with detected CO outflows. The far-infrared CO rotation temperatures of the detected PBRS are marginally colder ( $\sim 230$  K) than those observed for most protostars ( $\sim 300$  K), and only one of these 5 PBRS has detected [OI]  $63 \mu\text{m}$  emission. The high envelope densities could be obscuring some [OI] emission and cause a  $\sim 20$  K reduction to the CO rotation temperatures.

## 1. Introduction

The earliest stage of the star formation process is characterized by a dense, infalling envelope of gas and dust surrounding a nascent protostar. This early phase, in particular, is known to be associated with powerful outflows (Arce et al. 2007; Frank et al. 2014). These outflows may ultimately play a role in halting the mass infall process and dispersing the envelope (Arce & Sargent 2006), thereby contributing to the overall low efficiency of the star formation process (Offner & Arce 2014). These outflows develop rapidly and with velocities of  $\sim 10 - 100 \text{ km s}^{-1}$  the outflows may propagate by 0.1 pc in 10,000 yr - 1,000 yr timescales. Therefore, outflows are important to characterize at the youngest possible ages in order to understand their early evolution.

The youngest identified protostars are known as Class 0 sources (Andre et al. 1993); they are distinguished from more-evolved Class I sources by their cold bolometric temperatures ( $T_{bol} < 70$  K; (Myers & Ladd 1993)) and/or ratio of submillimeter luminosity ( $L_{submm}$ ) to bolometric luminosity ( $L_{bol}$ ) being  $> 0.5\%$ . These diagnostics indicate that Class 0 sources typically have denser and more massive infalling envelopes than Class I sources. In addition to the Class 0 sources, an earlier phase of the star formation process has been postulated, the first hydrostatic cores (FHSC; e.g., Larson 1969). A number of candidate FHSCs have been identified (Enoch et al. 2010; Chen et al. 2010; Pineda et al. 2011; Schnee et al. 2012); moreover, candidate FHSCs have quite low luminosities and bear some similarity to the *Spitzer*-identified very low-luminosity sources (VeLLOs Young et al. 2004; Dunham et al. 2006). The exact nature of the VeLLOs and candidate FHSCs remains unclear as it is difficult to distinguish bonafide FHSCs from sources that will go on to form very low mass stars (Dunham et al. 2014).

As part of the *Herschel* Orion Protostar Survey (HOPS) (e.g., Fischer et al. 2010; Stanke

et al. 2010; Ali et al. 2010; Manoj et al. 2013; Furlan et al. 2016), a sample of 19 protostars with bright 70  $\mu\text{m}$  and 160  $\mu\text{m}$  emission and correspondingly faint or undetected (8 sources) 24  $\mu\text{m}$  emission were detected in the Orion star forming region (Stutz et al. 2013, hereafter ST13). We refer to these protostars as the PACS Bright Red Sources (PBRs); of the 19 PBRs, 12 were first identified as protostars by *Herschel* and 7 *Spitzer*-identified protostars also fulfilled the 24  $\mu\text{m}$  to 70  $\mu\text{m}$  color criteria (ST13). The PBRs are *not* low-luminosity like the VeLLOs and candidate FHSCs; they have bolometric luminosities ( $L_{bol}$ ) ranging between 0.65  $L_{\odot}$  and 30.6  $L_{\odot}$ , with a median  $L_{bol}$  of  $\sim 3 L_{\odot}$ . Thus, the PBRs are the largest sample of extremely young protostars with typical luminosities; the median luminosity of Class 0 protostars is 3.5  $L_{\odot}$  in Orion and 1.4  $L_{\odot}$  in the nearby clouds (Dunham et al. 2014). While the PBRs have only been well-characterized in Orion, similar examples are present in more nearby clouds (e.g., VLA 1623, IRAS 16293-2422), and Sadavoy et al. (2014) identified several protostars in Perseus that were not classified as protostars in *Spitzer* or undetected at 24  $\mu\text{m}$  (i.e., HH211-mms Rebull et al. 2007).

We further characterized the envelopes of 14 PBRs using observations of the 2.9 mm dust continuum (Tobin et al. 2015); that study, hereafter Paper I, focused specifically on the most deeply embedded and *Herschel*-identified sources. The observed PBRs were all detected and found to have among the largest 2.9 mm luminosities of known Class 0 protostars. We also found that 6 out of 14 have visibility amplitudes that are flat within increasing uv-distance. The flat visibility amplitudes indicate that the 2.9 mm emission is very concentrated, and this finding, together with the high 2.9 mm luminosities, confirms that most PBRs have dense envelopes. This corroborates the interpretation of the spectral energy distribution (SED) model comparisons in ST13. The characterization of the PBRs from both the SEDs and millimeter continuum have led us to conclude that the PBRs may be among the youngest Class 0 objects. If the PBRs represent a distinct portion of early Class 0 evolution, as suggested by ST13, then the relative numbers of PBRs to Class 0 sources in Orion indicates that a ‘PBRs phase’ could last  $\sim 25,000$  yr. This estimate assumes that the Class 0 phase lasts  $\sim 150,000$  yr (Dunham et al. 2014).

A remaining source of uncertainty in the interpretation of the PBRs as the youngest Class 0 protostars is their unknown disk/envelope inclination angles with respect to the plane of the sky. There is a degeneracy between high envelope densities versus high (nearly edge-on) inclinations that could not be mitigated due to the lack of emission shortward of 10  $\mu\text{m}$  toward most PBRs (e.g., Whitney et al. 2003; Furlan et al. 2016). Assuming that outflows are perpendicular to the disk or envelope midplanes, observations of outflows to constrain their orientations (e.g., in molecular lines) are an excellent way to estimate disk/envelope inclinations and further constrain the envelope properties. Furthermore, if the PBRs are among the youngest Class 0 protostars, then the sample as a whole represents an opportunity

to examine the outflow properties of the youngest protostars.

The jets and outflows from protostars are detected with a variety of complementary methods and the types of outflows and the ways to detect them also vary with evolution. Collimated jets detected in optical or near-infrared line emission are typically associated with more evolved Class I or Class II sources (Reipurth et al. 1997, 2010, e.g., HH111), while Class 0 protostars typically have a molecular outflow observable in only millimeter lines of CO and other molecules (Arce et al. 2007; Frank et al. 2014). However, this does not mean there is no collimated jet emission, just that it may be undetectable due to high levels of obscuration. The molecular outflow emission toward some low-mass protostars has an angular dependence of velocity, with low-velocity material at the edges of the outflow cavity and velocities as high as  $\sim 100 \text{ km s}^{-1}$  along the main axis of the outflow (e.g., Santiago-García et al. 2009; Hirano et al. 2010). Jet-like features can also be seen in shock-tracing molecules such as SiO and SO (e.g., Lee et al. 2008, 2009). The velocity gradients along the outflow axis also offer crucial information of disk-protostar orientation (e.g., Cabrit & Bertout 1986; Lee et al. 2000).

Far-infrared spectroscopy with the *Infrared Space Observatory* and the *Herschel Space Observatory* has also been found to be an excellent probe of the physical conditions of outflows from young stars. The high-J CO ( $J_u > 13$ ) and H<sub>2</sub>O transitions, in addition to OH and [OI] transitions, probe the warm and hot outflow conditions on scales very near the protostar and the jet driving source (e.g., van Kempen et al. 2010; Karska et al. 2013; Green et al. 2013; Manoj et al. 2013). The lines are thought to be excited primarily by shocks (Manoj et al. 2013), with UV radiation photo-dissociating H<sub>2</sub>O, causing lower abundances relative to non-irradiated shock models (Karska et al. 2014).

The initial development of the outflows and their subsequent breakout from their surrounding envelopes are still quite uncertain. Outflows have also been detected from VeLLOs and candidate FHSCs (Dunham et al. 2011; Pineda et al. 2011; Schnee et al. 2012; Tobin et al. 2015). Theory has predicted that such young objects can indeed produce the slow outflows ( $\sim 2 - 7 \text{ km s}^{-1}$ ) that have been observed (Price et al. 2012), and the outflows may develop prior to the formation of a rotationally-supported accretion disk (e.g., Li et al. 2013, 2014). However, it is still uncertain how quickly more powerful outflows emerge in protostars; do the outflows have a steady growth in power as the source luminosity (from accretion) increases or do they only become powerful once a certain threshold in luminosity is reached?

In order to examine the outflow conditions from the youngest known Class 0 protostars, we have obtained interferometric observations of the CO ( $J = 1 \rightarrow 0$ ) molecular line and far-infrared spectroscopy with the *Herschel Space Observatory* toward the PBRs in the

Orion A and B molecular clouds. The youth and number of PBRs in Orion offers an unique opportunity to examine the properties of outflows toward objects that are consistent with being among the youngest protostars. Furthermore, spectrally and spatially resolved observations of the molecular outflows toward these protostars will enable us to constrain the range of possible inclination angles of the protostellar sources, ensuring that their characterization as the youngest protostars is not strongly influenced by orientation.

We have observed 14 PBRs (from the full sample of 19 cataloged by Stutz et al. (2013) and Paper I) with the Combined Array for Research in Millimeter-wave Astronomy (CARMA), focusing on the *Herschel*-detected PBRs sample. We observed the protostars in both the dust continuum and spectral line emission to examine the envelope and outflow properties of these sources. We discuss the observations in Section 2, our outflow results from CO ( $J = 1 \rightarrow 0$ ) and *Herschel* spectroscopy are presented in Section 3, we discuss the results in Section 4, and summarize our main conclusions in Section 5.

## 2. Observations and Data Reduction

### 2.1. CARMA Observations

We conducted observations toward 14 out of 19 of the PBRs identified in ST13 with CARMA in the D-configuration ( $\sim 5''$  resolution) during late 2012 and early 2014 and follow-up observations in C-configuration ( $\sim 2''$  resolution) for some in early 2014. The observations were conducted with the main CARMA array comprised of 6 - 10.4 m and 9 - 6.1 m antennas. We observed two or three sources per track and configured the correlator with four 500 MHz continuum windows, two 8 MHz windows to observe para-NH<sub>2</sub>D ( $J = 1_{11} \rightarrow 1_{01}$ ) and C<sup>18</sup>O ( $J = 1 \rightarrow 0$ ), and the two 31 MHz windows for observation of <sup>13</sup>CO ( $J = 1 \rightarrow 0$ ) and <sup>12</sup>CO ( $J = 1 \rightarrow 0$ ). The C-configuration observations had five 500MHz continuum windows because we did not observe para-NH<sub>2</sub>D in that configuration. The continuum observations were presented in Tobin et al. (2015) and here we will present only the <sup>12</sup>CO ( $J = 1 \rightarrow 0$ ) results because other lines did not yield strong detections. Our sensitivity is typically 0.15 Jy beam<sup>-1</sup> channel<sup>-1</sup> for the CO ( $J = 1 \rightarrow 0$ ) in 0.5 km s<sup>-1</sup> channels. We used standard procedures within the MIRIAD software package (Sault et al. 1995) to edit, reduce, and image the data; all maps were reconstructed with natural weighting. The CARMA observation log is given in Table 1. The absolute flux calibration uncertainty is  $\sim 10$ -20%. The largest angular scale that can be recovered from observations is  $\sim 20''$ ; we estimate this number to be twice the minimum baseline length.

## 2.2. *Herschel* PACS Spectroscopy Observations

We also observed 8 PBRs sources with the Photodetector Array Camera and Spectrometer (PACS; Poglitsch et al. 2010) on the *Herschel Space Observatory* (Pilbratt et al. 2010) as part of program OT2\_jtobin.2; we also observed the Class I protostar HOPS 347. The PACS spectrometer is a far-infrared integral field spectrograph with a  $5 \times 5$  spaxel (spatial pixel) foot print and spaxel sizes of  $9''$ , for more information see Poglitsch et al. (2010).

We conducted full range scans of the entire spectral range from  $\sim 55 \mu\text{m}$  to  $\sim 200 \mu\text{m}$  in standard chop-nod mode. Table 2 lists the observations dates and observations ids for the observed sources. The PACS range scan spectra were reduced using HIPE 13.0 SPG v11.1.0, calibration tree version 56. The root-mean-squared absolute flux calibration uncertainty of the PACS spectra is  $\sim 12\%$ .

The line spectroscopy observations of the [OI]  $63.18 \mu\text{m}$  transition were conducted in unchopped mode. The unchopped mode uses separately defined off positions away from the cloud to prevent corrupting the [OI] line with a contaminated off position in chop-nod mode. This mode was necessary because extended [OI] emission is very prevalent in the Orion molecular cloud. The use of unchopped mode will, however, result in foreground/background [OI] emission on the surrounding molecular cloud being preserved, in addition to that of the protostar itself. These observations were taken in bright line mode, which has less redundancy at each wavelength than faint line mode. The data used in this paper are the from the default archive reduction from science product generation version 12.1.0 and utilizing PACS calibration tree version 65.

In this paper, we are making use of the flux densities derived from the central spaxel, corrected for the point spread function losses. For flat-fielding, we use the observed relative spectral response function (RSRF) rather than the telescope background method.

## 2.3. Magellan Near-infrared Observations

We observed the source HOPS 68 with the Magellan Baade telescope, located at Las Campanas in Chile on 2009 January 17. The observations were conducted with the Persson Auxiliary Nasmyth Infrared Camera (PANIC, Martini et al. 2004), which has  $2' \times 2'$  field of view on a  $1024 \times 1024$  pixel detector. HOPS 68 was observed in Ks-band using a  $3 \times 3$  dither pattern with 20 second integrations at each dither position and  $15''$  steps between dither positions. The sky image was constructed from a median combination of the on-source frames thereby losing some large-scale emission. The data were reduced using the Image Reduction and Analysis Facility (IRAF) using standard methods for near-infrared imaging

observations; see Tobin et al. (2010) for a description of the methods used.

## 2.4. Sample and Sub-samples

The observations and results presented in this paper are based on sub-samples of the PBRS sample presented in ST13. ST13 identified 18 sources with  $[24\ \mu\text{m}] - [70\ \mu\text{m}]$  colors (in  $\log(\lambda F_\lambda)$  space) redder than 1.65. Of this sample, 11 were first discovered with *Herschel* observations and 7 were previously known HOPS protostars from the *Spitzer* surveys of the region that met the redness criteria. Furthermore, an additional PBRS (135003) was not included in ST13, but was first presented in Paper I, bringing the total number of PBRS to 19. We list the full sample of PBRS in Table 3 and identify those that have been followed-up with CARMA and *Herschel* PACS Spectroscopy. The CARMA follow-up concentrated primarily on sources that had not been previously identified by *Spitzer* as protostars due to their deeply embedded nature, rendering them faint or undetected at  $24\ \mu\text{m}$ . The *Herschel* PACS spectroscopy then concentrated on the *Herschel*-identified PBRS that had been found in the HOPS data that had been analyzed prior to the *Herschel* Open Time 2 proposal deadline. Thus, our source follow-up is not homogeneous, but there is enough overlap in order to identify characteristic trends within the sample and sub-samples which we will detail in the following sections.

## 3. Results

We have compiled a significant amount of data to further characterize the PBRS and their outflow properties. We will first discuss the cold molecular outflows probed by CARMA CO ( $J = 1 \rightarrow 0$ ) and probe scales beyond those examined by CARMA using *Spitzer*  $4.5\ \mu\text{m}$  emission. Lastly, we will discuss the results for the warm and hot components of the molecular outflows with *Herschel* PACS spectroscopy and place the properties of the PBRS outflows in the context of larger protostar samples observed with far-infrared spectroscopy. While the three datasets do not cover the same samples (see Table 3) and the spatial scales examined are different, they all contribute to a deeper understanding of the PBRS than when considered on their own. We will attempt to concentrate on overarching trends in the following discussion of results and the discussion of individual sources can be found in the Appendix.

### 3.1. Molecular Outflows

The  $^{12}\text{CO}$  ( $J = 1 \rightarrow 0$ ) molecular line was observed to examine the outflow activity toward each source; this is the canonical tracer of outflowing gas toward protostellar objects (Snell et al. 1980). Outflows are generally characterized by distinct red and blue-shifted emission located on either side of the protostellar source, modulo inclination effects. The pervasiveness of CO in the Orion molecular cloud complicates analysis of outflows. Emission at  $\pm 2 \text{ km s}^{-1}$  around the systemic velocity cannot be analyzed due to the  $^{12}\text{CO}$  ( $J = 1 \rightarrow 0$ ) emission being resolved-out due to confusion with the extended molecular cloud. Therefore, we are generally only able to detect outflow features that have velocities high enough to emit outside the  $\pm 2 \text{ km s}^{-1}$  velocity range.

#### 3.1.1. Detections and Morphologies

We detect clear CO outflows toward 7 PBRs sources 093005, 090003, 082012, 119019, 135003, HOPS 373 and 019004 (Figures 1, 2, 3, 4, 5, 6, & 7), as well as for the Class I source HOPS 68 in the field of 019003 shown in Figure 8. Tentative detections are found toward 3 additional PBRs 302002, 061012, and HOPS 372 (Figures 9, 10, & 3). The HOPS 372 outflow is apparent in the low-velocity panel of Figure 3, but at higher velocities the outflow emission is dominated by 082012. We did not detect outflow emission toward four PBRs 091015, 091016, 097002, and 082005; however, this does not mean that these sources do not have outflows, but that they were not detectable with our resolution and sensitivity.

The outflows have a variety of morphologies, there is not a typical CO outflow morphology toward the PBRs sources. The PBRs 093005 and 090003 have spatially compact outflows, with total lengths of the red and blue-shifted lobes being less than 0.05 pc (Figures 1 & 2). The outflows toward 119019, 082012, 135003, and HOPS 373 all extend outside the CARMA primary beam, with total lengths greater than 0.1 pc (Figures 3, 4, 5, and 6). The outflows toward 082012 and 135003 also have emission extending to velocities  $> \pm 10 \text{ km s}^{-1}$  from the systemic velocity with jet-like morphologies.

Toward 061012, there is evidence for an outflow, but this is unclear due to confusion with the wide-angle outflow of its neighbor HOPS 223 (Figure 10). HOPS 223 (also known as V2775 Ori) is an outbursting Class I source (Fischer et al. 2012) and this is the first clear detection of a CO outflow toward this source. However, the *Spitzer* imaging already showed strong evidence for outflow-associated features. Toward 302002 (Figure 9) there appears to be low-velocity  $^{12}\text{CO}$  emission in its vicinity that appears outflow-like, but its detection is not definitive.

The outflow toward 119019 is distinct from the other PBRs in that it has a large spatial extent, but at low-velocities; the full velocity width is only  $6 \text{ km s}^{-1}$  for both the red and blue sides of the outflow. Moreover, the spatial overlap between the redshifted and blueshifted emission is strong evidence that this source is viewed close to edge-on.

The non-detections of outflows toward 091015, 091016, 097002, and 082005 could result from the outflows having low-velocities and being confused with the emission from the molecular cloud. Also, there is a tentative trend between detectable outflows and  $L_{bol}$ . The PBRs 119019 was the lowest luminosity source ( $L_{bol} = 1.56 L_{\odot}$ ) with a clear outflow detection; the tentative outflow detections and non-detections have luminosities between  $0.65 L_{\odot}$  and  $1.56 L_{\odot}$ . The outflow properties of individual sources are described in more detail in the Appendix.

The outflow from HOPS 68 (Figure 8) is worth mentioning because it was also found to have quite high velocities, and the relative position angle of the red and blue-shifted lobes changes from high to low-velocity. At low velocities the outflow is oriented northeast to southwest, but at high velocities the red-shifted side is oriented northwest to southeast while the blue lobe still appears extended in the same direction as at low velocities. We overlaid the high-velocity CO contours on a Ks-band ( $2.15 \mu\text{m}$ ) image from Magellan PANIC (Figure 8) and we see that there are two sets of bow-shock features that overlap with the blue-shifted CO emission. One set of features is in the southeast direction and the other set is in the south west direction. Thus, the change in position angle of the CO emission from low to high velocities is likely indicative of two outflows from HOPS 68.

### 3.1.2. Outflow Parameters

We calculate the outflow mass, momentum, and energy following the procedure used by Plunkett et al. (2013) (based on Bally et al. 1999), and give these values in Table 4. The analysis by Plunkett et al. (2013) uses  $^{13}\text{CO}$  optical depths and excitation temperature derived from  $^{12}\text{CO}$  (assuming optically thick emission) in order to calculate column densities, from which the mass, momentum, and energy can be calculated. However, our observations did not have enough sensitivity to detect the  $^{13}\text{CO}$  ( $J = 1 \rightarrow 0$ ) outflow emission, we therefore adopted a  $^{12}\text{CO}/^{13}\text{CO}$  ratio of 62 (Langer & Penzias 1993) and divided the  $^{12}\text{CO}$  ( $J = 1 \rightarrow 0$ ) intensities by this ratio, under the assumption that the  $^{12}\text{CO}$  emission is optically thin at all velocities. This assumption is not valid at all velocities, but probably most reasonable for the higher velocity ( $> \pm 10 \text{ km s}^{-1}$ ) emission. The principal effect will be an underestimate of the CO column densities and cause all the outflow parameters to be lower limits. Dunham et al. (2014) showed that opacity corrections to the outflow parameters

can be up to an order of magnitude; missing flux will also affect the parameters but this is more difficult to quantify since the low-velocity emission with the highest opacity will be the most severely affected by spatial filtering. The  $^{13}\text{CO}$  abundance is taken to be  $N(^{13}\text{CO}) = N(\text{H}_2)/7 \times 10^5$  Frerking et al. (1982) and the excitation temperature is calculated using the  $^{12}\text{CO}$  brightness temperature and was between 15 K and 40 K in our observations (see Equation 3 in Plunkett et al. 2013). We do not attempt to correct the outflow properties for the effects on inclination.

The observed outflow properties (mass, momenta, energy, and force; see Table 4) of the PBRS are generally consistent with results from Plunkett et al. (2013); however, there is a general tendency for lower values of mass, momentum, and energy for the PBRS, which could result from the lack of  $^{13}\text{CO}$ . We also computed the outflow force ( $F_{\text{CO}}$ ) and dynamical time based on the apparent outflow size and the maximum velocity of observed CO. We examined the relationship between  $L_{\text{bol}}$  and  $F_{\text{CO}}$  in Figure 11. For the PBRS with a detected outflow, there is no clear correlation between  $F_{\text{CO}}$  and  $L_{\text{bol}}$ , but more luminous sources tend to have greater values of  $F_{\text{CO}}$ . We have also plotted the relationships derived by Bontemps et al. (1996) and van der Marel et al. (2013) for comparison. The relationships were derived from samples primarily comprised of Class I protostars and Class 0 protostars lie above the relationship and not below; the CO ( $J = 6 \rightarrow 5$ ) measurements from Yıldız et al. (2015) for Class 0 sources are also above the Bontemps et al. (1996) relationship. The relations do go through our observed the points, but four PBRS are found below the Bontemps et al. (1996) relationship. On the other hand we use interferometer data without zero-spacings, while the other studies used single-dish maps. We also did not have  $^{13}\text{CO}$  detections, making our values lower limits. We do not calculate upper limits for the sources with non-detections because the large amount of resolved emission near the source velocities results in these values having little physical meaning. However, their outflow parameters will (at a minimum) be lower than those measured for 090003/093005.

### 3.1.3. Outflow Inclinations

The outflow inclinations are difficult to precisely measure; however, we qualitatively compared our data with the simulations of Cabrit & Bertout (1986), which show model PV plots and integrated intensity plots for accelerating outflows. Model outflows are shown for a fixed opening angle and outflow length at inclinations of  $5^\circ$ ,  $30^\circ$ ,  $50^\circ$ , and  $80^\circ$ . As such, the uncertainty in our estimates of the outflow inclination is likely  $\pm \sim 20^\circ$ . The outflows of 090003, 093005, HOPS 223, and 019003 are consistent with an outflow inclinations near  $30^\circ$ , given their compact extent and distribution of highest velocities near the source. The

well-collimated outflows of 082012, 135003, and HOPS 68 appear most consistent with an inclination near  $50^\circ$ . Both the wide-angle outflow toward HOPS 373 and the tenuous outflow toward 302002 are consistent with having inclinations between  $50^\circ$  and  $80^\circ$ ; based on their velocity distributions, HOPS 373 is likely closer to  $50^\circ$ , while 302002 is likely closer to  $80^\circ$ . The PBRs 061012 appears to have an outflow, but the data do not lend themselves to a reasonable estimate of the inclination. Finally, 119019 is the only PBR that is consistent with having a near edge-on inclination, as indicated by the CO emission only being detected at low velocities and the extended spatial overlap of the red and blue-shifted emission toward 119019.

We can broadly conclude that for the PBRs with detected outflows, extreme edge-on orientations cannot be the cause of their extremely red  $24\ \mu\text{m}$  to  $70\ \mu\text{m}$  colors, except for 119019. The estimated inclinations for the PBRs are also given in Table 5. Furthermore, while there is a large degree in uncertainty in the outflow inclinations, it is most likely that the distribution of inclination angles appears dominated by intermediate inclinations ( $80^\circ \geq i \geq 20^\circ$ ). While our numbers are small, the distribution is likely consistent with a random distribution of inclinations (the average inclination for a random distribution is  $60^\circ$ ), which is expected for a collection of sources whose selection criteria is not particularly biased toward a particular geometric orientation; as had been a previous concern with respect to the PBRs was they could have simply been edge-on sources and the outflow data show that this is clearly not the case. Given the uncertainty in the inclination angles, we have not corrected the derived outflow parameters in Table 4 for this effect.

### 3.2. Evidence for Extended Outflows

The CARMA  $^{12}\text{CO}$  observations are only sensitive to emission within the  $30''$  (12600 AU) radius primary beam, hence other observations are needed to determine if the outflows extend to larger scales. We examined the *Spitzer*  $4.5\ \mu\text{m}$  images of all the sources from Megeath et al. (2012). The emission at  $4.5\ \mu\text{m}$  can trace both scattered light in the outflow cavities near the protostars and shock-excited  $\text{H}_2$  emission along the outflows. Smooth  $4.5\ \mu\text{m}$  emission near the source is likely indicative of scattered light and knotty or bow shock-like features along the outflow are likely  $\text{H}_2$  emission (e.g., Tobin et al. 2007). Images of the  $4.5\ \mu\text{m}$  emission are shown for all the sources in Figure 12a and 12b.

Toward the sources HOPS 373, 093005, 302002, and 090003 there is  $4.5\ \mu\text{m}$  emission within 0.05 pc of the sources and no apparent evidence for emission out on larger-scales that is likely to have originated from these systems. Thus, for 093005, 302002, and 090003 we are likely covering the full extent of the outflow with our CO observations; for HOPS 373,

however, the outflow extends out of the primary beam, but perhaps not much further (Gibb & Little 2000).

There are a few cases where the association of the 4.5  $\mu\text{m}$  emission with the outflow is ambiguous. For 135003, there are some knotty features along the direction of the known outflow, extending  $\sim 0.15$  pc and was identified as an outflow candidate (SMZ 1-38) by Stanke et al. (2002). Then in the case of 019003, we see a feature adjacent to the position of the protostellar source from the 2.9 mm continuum, and possibly an extended feature in the direction of the blue-shifted outflow lobe. The crowding and number of imaging artifacts from bright sources make this field difficult to interpret.

We only find clear evidence for 4.5  $\mu\text{m}$  emission extended  $> 0.1$  pc for three sources 082012, 061012, and 119019. The bow-shock directions or trail of  $\text{H}_2$  knots indicate a likely origin from the PBRs source. The emission from 061012 and 119019 appears to extend  $\sim 0.3$  pc and the emission from 082012 extends  $\sim 0.2$  pc. If we assume an outflow propagation speed of 10 - 100  $\text{km s}^{-1}$ , then the dynamical time is between 3000 - 30000 yr for 0.3 pc and 2000 - 20000 yr for 0.2 pc. Thus, even though there is evidence for outflows toward these sources extending relatively large distances, extreme youth is still likely.

Toward the sources without detected CO ( $J = 1 \rightarrow 0$ ) outflows, 091015, 091016, 082005, and 097002, there is also no evidence for 4.5  $\mu\text{m}$  emission (or emission shortward of 70  $\mu\text{m}$ ) associated with the sources, as shown in (see Figure 12a and 12b). Whereas, the sources with compact emission at 4.5  $\mu\text{m}$  also had detections of CO outflows.

### 3.3. Warm/Hot Outflow Gas

We obtained *Herschel* PACS spectroscopy toward a subset of the PBRs (eight observed with PACS). This subset samples luminosities between 0.65  $L_\odot$  and 12  $L_\odot$  and a variety of  $^{12}\text{CO}$  molecular outflow emission properties; thus, this subsample should be reasonably representative of the PBRs as a whole. PACS spectroscopy offers a complementary view of the outflow emission from protostars; rather than the cold, entrained gas traced in the CO ( $J = 1 \rightarrow 0$ ) line, the PACS lines trace the warm/hot shock-heated portion of the outflow concentrated on scales  $< 2000$  AU.

The continuum-subtracted PACS spectra for all observed sources, extracted from the central spaxel, are shown in Figure 13. The spectra have a wide variety of emission line strengths; detections in high-J CO and water are found toward 5 out of the 8 PBRs. The spectrum toward HOPS 373 is particularly strong and rich in line emission, detecting CO transitions with  $J_u > 30$ . Also, lines in the PACS spectrometer range are detected toward

all sources that exhibit a clear outflow in the CO ( $J = 1 \rightarrow 0$ ) transition. We calculate the total high-J CO luminosities and give their values in Table 6.

Figure 14 shows the non-continuum subtracted CO ( $J = 14 \rightarrow 13$ ) spectra for the all observed sources. The PBRs 061012 has a tentative detection ( $2.5\sigma$ ) in the CO ( $J = 14 \rightarrow 13$ ) line, while its detection was not immediately apparent in the full spectrum shown in Figure 13. However, 061012 does not have detected emission in the  $179.5 \mu\text{m}$  H<sub>2</sub>O  $2_{12}-1_{01}$  line which typically has a line flux greater than or equal to the CO ( $J = 14 \rightarrow 13$ ) line. Thus, the detection toward 061012 is considered tentative.

Observations were also obtained toward all the PBRs in unchopped line spectroscopy observations of the [OI]  $63.18 \mu\text{m}$  transition. This emission line is thought to be a tracer of the protostellar jet, perhaps even before the molecular outflow is well-established (Hollenbach & McKee 1989). Since these observations were conducted in the unchopped mode, extended [OI] emission from the cloud is present in the spectral cubes. This extended [OI] emission from the cloud must be subtracted from the data in order to isolate [OI] emission from the protostar itself. To remove the extended [OI] (and continuum emission), we have calculated the median intensity at each wavelength in the spectral cube using the 18 edge spaxels. We also compute the standard deviation of the edge spaxel intensities at each wavelength, this is representative of the uncertainty in the background emission subtracted at each wavelength. We use the median intensity of the edge spaxels rather than the mean because some spaxels have very high intensities and the mean would be skewed toward a value larger than most of the edge spaxel intensities. The background subtracted [OI] spectra are shown toward each source in Figure 15 as the thick solid line and the standard deviation of the background at each wavelength is shown as the thin dashed line in Figure 15.

The only PBRs with a clear detection of the [OI] line is HOPS 373; 019003 at first glance appears to have a detection, but it is  $\sim 2\sigma$  above the uncertainty of the subtracted background [OI] emission, so this detection is tentative. Furthermore, 119019 and 061012 have apparent peaks at location of the [OI] line; however, both of these are only  $2\sigma$  detections above the noise and other features are found in those spectra with the same significance, but do not correspond to an expected spectral feature. Therefore, neither of these sources are regarded as detections.

Nisini et al. (2015) showed a sample of protostellar sources with extended [OI] emission in their jets and outflows. This highlights the possibility that some of the PBRs may have extended emission along their outflows, and that our subtraction of background [OI] emission from the edge spaxels may remove [OI] emission from the source. However, we inspected the spectral cubes before and after subtraction of extended [OI] emission, and we do not detect any enhancement of [OI] emission along the outflow directions (for the PBRs with

detected outflows), nor do the 8 pixels adjacent to the central spaxel show emission after background subtraction toward HOPS 373. Therefore, we conclude that the well-detected emission toward HOPS 373 is only detected in the central spaxel and we are not missing extended flux at our sensitivity ( $\sigma_{[\text{OI}]} \sim 1 \text{ Jy channel}^{-1}$ ), and we are not subtracting off extended emission associated with the PBRS outflows.

We have examined the [OI] line luminosities with respect to larger protostar samples from (Green et al. 2013) and Mottram et al. (2016, submitted). The  $\sim 2\sigma$  [OI] detections for 119019 and 062012 and  $3\sigma$  upper limits for 093005, 091015, and 091016 have [OI] luminosities upper limits consistent with the detected range of [OI] luminosities for a given  $L_{bol}$  ( $L_{[\text{OI}]} = 10^{-5} - 10^{-2} L_{\odot}$ ; Green et al. 2013). Thus, the [OI] line is not found to be particularly strong toward the PBRS, but we cannot say that the [OI] emission anomalously weak toward the PBRS given that the upper limits do not indicate [OI] luminosities to be significantly lower than other protostars with a similar  $L_{bol}$ .

In addition to the [OI] 63.18  $\mu\text{m}$  line, we examined the spectra for [OI] emission at 145.5  $\mu\text{m}$  in the range scans. As shown in Figure 13, this line is only detected toward 019003. However, we do not think this is emission from the protostar itself, but extended emission that was not fully subtracted from the off position as some spaxels have a negative feature, while others have emission.

The [OI] 63  $\mu\text{m}$  luminosity from post-J-shock gas can be used to calculate the mass flow rate through the shock (Hollenbach & McKee 1989; Hollenbach 1985):  $\dot{M} = L([\text{OI}]) \times 8.1 \times 10^{-5} M_{\odot} \text{ yr}^{-1} L_{\odot}^{-1}$ . Since our observations encompass, in each case, all the regions in which the outflows from our targets drive shocks. Thus, the result is the mass-loss rate from the protostar, averaged over the outflow dynamical time. The [OI] luminosities and outflow rates inferred from the line luminosities (and their upper limits) are given in Table 6.

### 3.3.1. *Extended emission*

The high-J CO and water line emission is extended across multiple spaxels in some sources, the most obvious of which is 135003. We overlay the spectra in each spaxel on the CO ( $J = 1 \rightarrow 0$ ) map in Figure 16a for the longer and shorter wavelength ends of the PACS spectrometer red channel. H<sub>2</sub>O and CO emission is detected in all spaxels that overlap with the blue-shifted side of the CO ( $J = 1 \rightarrow 0$ ) outflow, and the line emission is actually brighter than that of the central spaxel. However, there is not corresponding line emission extended along the red-shifted side of the outflow, possibly indicating that the southern side of the outflow is being driven into a less-dense medium. Similarly, 019003 also has some

extended H<sub>2</sub>O and CO emission on the blue-shifted side of the CO ( $J = 1 \rightarrow 0$ ) and like 135003 the extended emission is also brighter than the central spaxel.

### 3.3.2. CO Luminosities and Rotation Temperatures

We have calculated the high-J CO luminosities and rotation temperatures for the 5 PBRS with multiple detected CO transitions. We calculate the column densities of each CO line and luminosity of each line following Manoj et al. (2013); however, instead of fitting Gaussian functions to the unresolved line profiles, we directly sum the spectral elements around the wavelength of a particular CO line and subtract the background emission estimated from line-free continuum regions adjacent to the emission line. We regard this method as more reliable than fitting Gaussians given the low spectral resolution of the data; similar results are obtained for the Gaussian method, however (Manoj et al. 2016 submitted).

We show the rotation diagrams for the 5 sources with robust CO detections in multiple lines in Figure 17. All sources show the characteristic warm component ( $\sim 300$  K) of the CO rotation diagrams (e.g. van Kempen et al. 2010; Karska et al. 2013) and only HOPS 373 shows evidence of another temperature component in CO lines with  $J_u \geq 25$ ; all other PBRS have non-detections for CO lines with  $J_u \geq 25$ . Thus, we fit a linear slope to the rotation diagrams for all detected CO lines with  $J_u \leq 25$ , finding  $T_{rot}$  between 216 K and 282 K. HOPS 373 has the highest  $T_{rot}$  and 119019 has the lowest  $T_{rot}$ .

We plot the PACS CO luminosities ( $L(\text{CO})$ ) versus  $L_{bol}$  and  $T_{bol}$  in Figure 18. The PBRS have CO luminosities that are consistent with the observations from the HOPS, WISH, WILL and DIGIT<sup>2</sup> samples (Karska et al. 2013; Manoj et al. 2013; Green et al. 2013; Karska et al. 2014, Mottram et al. submitted; Karska et al. in prep.)<sup>3</sup>. However, HOPS 373 has nearly the highest CO line luminosity for all protostars in the samples considered here for protostars with  $L_{bol} < 30 L_{\odot}$ . Looking at  $L(\text{CO})$  vs.  $T_{bol}$ , also in Figure 18, the PBRS are comparable to other sources with low values of  $T_{bol}$ .

The comparison of CO  $T_{rot}$  to the HOPS/WISH/WILL/DIGIT samples is shown in Figure 19; these rotation temperatures are all measured using CO lines with  $14 \leq J_u \leq 25$ .

---

<sup>2</sup>WISH stands for Water In Star forming regions with *Herschel*, WILL stands for William Herschel Line Legacy, and DIGIT stands for Dust, Ice, and Gas, In Time. WISH and DIGIT were *Herschel* key programmes and WILL was an Open Time 2 programme.

<sup>3</sup> The PACS CO data to be published in Karska et al. is a synthesis and updated analysis of the WISH, WILL, and DIGIT data, while Mottram et al. focuses on the [OI], HIFI, and ground-based low-J CO observations of the WILL survey only.

The PBRS have  $T_{rot}$  values that are among the lowest observed for all protostars in the other sample at any luminosity. However, given the uncertainties in our own measurements and those in the literature, the PBRS are consistent with the observed distribution of  $T_{rot}$ , but on the low-side of the distribution. We discuss the possible causes for the PBRS have lower  $T_{rot}$  values further in Section 4.4.

### 3.3.3. Far Infrared Line Ratios

We calculated diagnostic line ratios that have been used by Karska et al. (2014) to compare the WISH and WILL observations with various shock models (Kaufman & Neufeld 1996; Flower & Pineau Des Forêts 2010; Flower & Pineau des Forêts 2015) and list them in Table 7 for the sources with detected lines. For most ratios, the values calculated for the PBRS are either within the range observed in the WISH/WILL samples (Karska et al. 2014) or the values are within  $1\sigma$  of the observed range. The primary line ratio that is systematically different from the WISH/WILL samples is the CO ( $J = 16 \rightarrow 15$ )/CO ( $J = 21 \rightarrow 20$ ); the ratios are systematically larger for all the PBRS. This likely reflects the colder CO  $T_{rot}$  values that are derived for the PBRS, relative to the WISH/WILL sources. We also list ratios for CO ( $J = 17 \rightarrow 16$ )/CO ( $J = 22 \rightarrow 21$ ), CO ( $J = 16 \rightarrow 15$ )/CO ( $J = 17 \rightarrow 16$ ), and CO ( $J = 21 \rightarrow 20$ )/CO ( $J = 22 \rightarrow 21$ ) because CO ( $J = 17 \rightarrow 16$ ) and CO ( $J = 22 \rightarrow 21$ ) are also accessible from SOFIA<sup>4</sup>.

One source, HOPS 373, also had detections of OH transitions, enabling further comparison to the WISH/WILL results. Note that one of the OH 84  $\mu\text{m}$  doublet lines is contaminated by CO ( $J = 31 \rightarrow 30$ ) and to correct for this we measured the flux of the uncontaminated doublet line and multiplied its flux by two. The ratio of OH 84  $\mu\text{m}$  to OH 79  $\mu\text{m}$  is larger than WISH/WILL, but within the uncertainties, H<sub>2</sub>O ( $4_{04}-3_{13}$ ) to OH 84  $\mu\text{m}$  is consistent with WISH/WILL, and CO ( $J = 16 \rightarrow 15$ ) to OH 84  $\mu\text{m}$  is slightly in excess of the WISH/WILL results. Thus, for HOPS 373, the H<sub>2</sub>O line emission relative to OH is weaker than predicted by the shock models, consistent with the suggested interpretation of Karska et al. (2014) that UV irradiation of the shocks is needed in order to explain the H<sub>2</sub>O and OH line ratios as suggested by Karska et al. (2014).

---

<sup>4</sup>Stratospheric Observatory For Infrared Astronomy <https://www.sofia.usra.edu/>

## 4. Discussion

The PBRS have been demonstrated, through multiple lines of evidence, to be consistent with being the youngest known Class 0 protostars. Their SEDs indicate that they are surrounded by very dense envelopes (ST13) and this was further confirmed by the CARMA 2.9 mm dust continuum luminosities (Paper I). If these sources truly are a sample of the youngest protostars, the results from the outflow diagnostics presented here can offer valuable clues to the properties of outflows toward very young protostars. Given the multitude of the data presented, including the continuum results from Paper I, we have compiled a list of PBRS properties determined from the follow-up observational data and present a summary of these data in Table 5.

### 4.1. Nature of the PBRS Very Red Colors

A principal uncertainty in the characterization of the PBRS was if the extremely red 24  $\mu\text{m}$  to 70  $\mu\text{m}$  colors observed by ST13 were strongly influenced by source viewing angle. If the PBRS were typical Class 0 sources and observed in exactly edge-on orientation, then the combined opacity of the envelope and disk midplane could result in the very red 24  $\mu\text{m}$  to 70  $\mu\text{m}$  colors. However, ST13 showed that even if the PBRS were all viewed edge-on, the envelope densities would still have to be  $>2\times$  higher than typically found toward HOPS protostars; the median envelope density for Class 0 protostars in HOPS at a radius of 1000 AU is found to be  $5.9 \times 10^{-18} \text{ g cm}^{-3}$  from SED modeling (Furlan et al. 2016).

For the sources with detected CO ( $J = 1 \rightarrow 0$ ) outflows, the clear spatial separation of the blue and redshifted CO emission clearly shows that 093005, 090003, 082012, HOPS 372, HOPS 373, 135003, 019004 are *not* observed with edge-on orientation and must be observed at an intermediate viewing angle (neither edge-on nor face-on). The distribution of inclinations is consistent with being random; therefore, the extremely red colors of these protostars are not the result of extreme edge-on viewing angle, but are due to the high density of the infalling envelope itself. We are unable to make a definitive conclusion about 061012 since the outflow is not clearly detected, but there appear to be separated blue and red lobes.

However, for two sources, 119019 and 302002, only low-velocity CO emission is found for those outflows. The outflow toward 302002 (Figure 9) had a small velocity gradient from across the source, and we mentioned in Section 3.1.3 that the inclination is likely between  $50^\circ$  and  $80^\circ$ , but closer to  $80^\circ$ . In the more extreme case of 119019, this PBRS had no detectable velocity gradient and there is roughly equal amounts of emission at both blue and redshifted

velocities (Figure 4). Thus, these two sources may only have been classified as PBRS because their of edge-on (or nearly edge-on) orientation.

In summary, we confirm that the extremely red colors of the PBRS are not the result of inclination for 7 out of 9 sources with detected CO ( $J = 1 \rightarrow 0$ ) outflows. The sources without detections of CO ( $J = 1 \rightarrow 0$ ) outflows may have low-velocity outflows that are confused with the cloud emission, or the outflows are still too small in spatial extent and are not bright enough to detect with the sensitivity of our current observations.

## 4.2. Outflow Properties

The outflows exhibit a range of masses, momenta, energies, and forces; HOPS 373 has outflow properties typical of those in Plunkett et al. (2013) and 082012 has outflow properties in excess (Table 4). In contrast, the two most compact outflows in the sample (090003 and 093005) have quite low outflow masses, momenta, energies, and forces. Since the Plunkett et al. (2013) sample includes single-dish data to measure the total flux, a comparison with Arce & Sargent (2006), using interferometer-only data, is more appropriate. The ranges for the observed outflow parameters from Arce & Sargent (2006) and Plunkett et al. (2013) are given in Table 4. We note, however, that neither of those studies computed  $F_{CO}$ . The sources 093005, 090003, and 302002 have values all less than the range from Arce & Sargent (2006), HOPS 223 is within the range, and HOPS 373 and 082012 have values in excess of these numbers.

The outflow toward 082012 is truly exceptional, its high-velocity nature was first reported by Sandell et al. (1999); it is more energetic and has more momentum than the strongest outflows in the Plunkett et al. (2013) sample. The increased collimation and large velocity extent bears resemblance to NGC 1333 IRAS 4A, L1448C (Hirano et al. 2010), and IRAS 04166+2706 (Santiago-García et al. 2009). This outflow has energies and momenta in excess of all the outflows observed by Arce & Sargent (2006) and Plunkett et al. (2013), but it is comparable to L1448C (Hirano et al. 2010). The outflow of 082012 is likely even more powerful than we measure it to be, given that our properties are lower-limits due to lack of  $^{13}\text{CO}$  observations to determine the optical depth and because we do not cover the full extent of the outflow. The outflow of 082012 is also likely blended with that of HOPS 372 at low velocities, but at higher velocities it appears to only come from 082012. Even if we are measuring the combined outflow properties, it is very strong relative to those observed in the nearby star forming regions.

The outflows from 090003 and 093005 represent the most compact (i.e., shortest) CO

outflows found in our data. The outflows of 093005 and 090003 are not observed to extend further than their apparent envelope sizes observed at  $870 \mu\text{m}$ . This and the compact  $4.5 \mu\text{m}$  emission may indicate that the outflows are just beginning to break out from their dense, natal envelopes. These outflows are not particularly powerful either, the outflow forces plotted in Figure 11 are on the low-end for Class 0 sources and 090003 is lower than the linear relationship from Bontemps et al. (1996), above which all Class 0s lie in current data (Yıldız et al. 2015, Mottram et al. submitted). Furthermore, the well-developed outflow from 135003 is also found to lie below the  $L_{bol}$  vs.  $F_{CO}$  relationship. Alternatively, the outflows could be more powerful, but since their energies and momenta are calculated using entrained material, observed CO ( $J = 1 \rightarrow 0$ ), the outflows only appear weak with these measures.

The deeply embedded sources without  $4.5 \mu\text{m}$  emission or outflow detections (097002, 091015, 091016, and 082005) may have outflows that are too weak/faint to detect in our observations. However, the lack of outflow detections toward these most embedded sources and the lack of particularly powerful outflows from 093005 and 090003, could indicate that outflows may be weak during the early Class 0 phase, given the apparent youth of the sources and small spatial extent of the outflows. Thus, it is possible that the outflow momentum/energy/force may be initially small early-on and are rising early in the Class 0 phase such that the Class 0 outflows will be systematically more powerful than Class I outflows (e.g., Bontemps et al. 1996; Yıldız et al. 2015). Weak initial outflows from protostars are predicted from simulations of the FHSC phase (Tomida et al. 2013; Price et al. 2012) where the outflows are  $<15 \text{ km s}^{-1}$ . If the PBRs have recently transitioned out of the FHSC phase, then they may not have reached their full outflow power as of yet. This will be further studied using single-dish data by Menenchella et al. (in prep.).

The absence of detected outflow activity in CO ( $J = 1 \rightarrow 0$ ) toward the four sources mentioned above cannot be construed as evidence of outflow absence because of our finite resolution and sensitivity. For example, the outflow toward OMC MMS6N (also known as HOPS 87) was only detected when it was observed at the highest resolutions with the SMA (Takahashi et al. 2012), due to its very small spatial extent. Thus, the non-detected outflows could be very compact and in the process of breaking out from the envelopes, necessitating higher resolution data. On the other hand, OMC MMS6N did have strong  $\text{H}_2\text{O}$  and CO emission lines observed in the far-infrared spectrum from *Herschel* (Manoj et al. 2013) and 091015/091016 had no detected emission lines in their PACS spectra. In contrast, 091015/091016 are low-luminosity sources ( $L=0.65 L_{\odot}$  and  $0.81 L_{\odot}$ ) and OMC MMS6N is a higher-luminosity source ( $L >30 L_{\odot}$ ), making direct comparisons between the sources difficult.

### 4.3. Relationship of Outflows and 2.9 mm Continuum Properties

In Paper I, the 2.9 mm continuum luminosities and visibility amplitude profiles were analyzed. We found that most PBRs had 2.9 mm continuum luminosities (median of  $1.0 \times 10^{-5} L_{\odot}$ ) and  $L_{2.9mm}/L_{bol}$  ratios (median of  $8.8 \times 10^{-6}$ ) greater than most nearby Class 0 protostars, which have a median  $L_{2.9mm} = 3.2 \times 10^{-6} L_{\odot}$  and a median  $L_{2.9mm}/L_{bol} = 8.5 \times 10^{-7}$ . The nearby Class 0 continuum samples are drawn from Tobin et al. (2011), Looney et al. (2000), and Arce & Sargent (2006), which are sensitive to comparable spatial scales;  $L_{2.9mm}$  is calculated assuming a 4 GHz bandwidth centered at 2.9 mm. The PBRs have a median  $L_{2.9mm}$  that is  $3 \times$  larger than typical Class 0s and  $L_{2.9mm}/L_{bol}$  that is  $10 \times$  larger. This means that the more nearby Class 0 protostars with high  $L_{2.9mm}$  also have a high  $L_{bol}$ , whereas the PBRs tend to have lower  $L_{bol}$ . Furthermore, the highest  $L_{2.9mm}$  for nearby Class 0 protostars is  $2.9 \times 10^{-5} L_{\odot}$  toward NGC 1333 IRAS 4A, in contrast to the highest  $L_{2.9mm}$  of  $3.4 \times 10^{-5} L_{\odot}$  for the PBR 082012; see Figure 2 from Paper I. Finally, 6 out of 14 PBRs (093005, 090003, 091016, 091015, 097002, and 082005) had flat visibility amplitude profiles (and small 5 k $\lambda$  to 30 k $\lambda$  visibility amplitude ratios), consistent with most emission being emitted from scales  $< 2000$  AU (Figures 3 and 4 from Paper I). Thus, the PBRs tend to have more massive envelopes relative to their bolometric luminosities as compared to other Class 0 sources and the flat visibility amplitude ratios indicate high densities in the inner envelopes (Paper I).

Here we more closely examine the two PBRs that have apparent inclination angles that are close to edge-on: 119019, being almost exactly edge-on, and 302002 being near  $80^{\circ}$  (between  $50^{\circ}$  to  $80^{\circ}$ ). The PBR 119019 has  $L_{2.9mm}/L_{bol}$  ( $1.47 \times 10^{-6}$ ) and  $L_{2.9mm}$  ( $2.3 \times 10^{-6} L_{\odot}$ ) values consistent with typical Class 0 protostars from the literature. Thus, in addition to having an nearly edge-on outflow, the 2.9 mm continuum emission from 119019 is not consistent with it having a massive, dense envelope like the rest of the PBRs (Table 5). This points to 119019 perhaps being more evolved than the rest of the PBRs and its very red colors can be attributed to an edge-on inclination. On the other hand, 302002 has values of  $L_{2.9mm}/L_{bol}$  ( $1.2 \times 10^{-5}$ ) and  $L_{2.9mm}$  ( $1.0 \times 10^{-5} L_{\odot}$ ) consistent with rest of the PBRs. Both of these sources also have declining visibility amplitudes (Paper I).

We also find a tendency for the PBRs with flat visibility amplitudes to show either a compact outflow or have no detectable outflow in the CO ( $J = 1 \rightarrow 0$ ) line and *Spitzer* 4.5  $\mu\text{m}$  emission. We suggested in Paper I that the PBRs with flat visibility amplitudes might be less-evolved than the PBRs with more rapidly declining visibility amplitudes. The sources with rapidly declining visibility amplitudes tend to have more extended, well-developed outflows (i.e., 082012, HOPS 373, and 119019) than sources with flat visibility amplitudes. Therefore we suggest that the flat visibility amplitude sources have outflows that are only beginning to break out of their envelopes. Thus, the PBRs with flat visibility

amplitudes may indeed be the initial stages of the Class 0 protostellar phase.

The change in visibility amplitude profile could be related to the outflows carving out cavities and lowering the overall mass of the inner envelope. On the other hand, if the inner envelope mass is rapidly accreted onto the protostar, then the visibility amplitude profiles would also dramatically decline. Using the example from Paper I, the free-fall time of  $2 M_{\odot}$  confined to a constant density sphere with  $R = 1500$  AU is only the  $\sim 10,000$  yr, quite short on the timescale of protostellar collapse. For the case of inside-out collapse (Shu 1977), the rarefaction wave would take  $\sim 36,000$  yr to propagate out 1500 AU (assuming a sound speed of  $0.2 \text{ km s}^{-1}$ ), the boundary of the rarefaction wave is where the density profile changes from  $r^{-2}$  to  $r^{-1.5}$ , reflecting free-fall collapse. Moreover, in the case of strong rotation, a portion of the density profile inside of the rarefaction wave can have a density profile of  $r^{-0.5}$  (Cassen & Moosman 1981; Terebey et al. 1984). Thus, in either case, the density structure of the inner envelopes can be significantly altered on a timescale shorter than the Class 0 phase ( $\sim 150,000$  yr, Dunham et al. 2014). Thus, the outflow detection and extents may simply correlate with the decrease in the visibility amplitude profiles and not cause it.

Lastly, the only flat visibility amplitude source with detected far-infrared line emission is 093005; only continuum emission was detected toward 091015 and 091016. The remaining sources with line emission had declining or uncertain visibility amplitude profiles.

#### 4.4. Far-Infrared Diagnostics in the Context of the PBRs

A key finding of our study is that in the absence of other outflow indicators (CO ( $J = 1 \rightarrow 0$ ), *Spitzer*  $4.5 \mu\text{m}$  scattered light/ $\text{H}_2$ ), the PACS line emission (CO,  $\text{H}_2\text{O}$ , or [OI]) does not independently show evidence for outflows in the form of shocks from the inner envelopes of the protostars. Thus, we only find far-infrared line emission toward sources that have detected CO ( $J = 1 \rightarrow 0$ ) outflows. This hints at a strong link between the mechanisms that produce the cold CO outflows and the warm/hot component observed in the far-infrared. Furthermore, the [OI]  $63 \mu\text{m}$  transition is only convincingly detected toward 1 PBRs (HOPS 373) out of the 6 PBRs for which we could reliably subtract the background [OI] emission from the edge spaxels. We do not consider the detections and non-detections of 135003 and 019004 meaningful because of the strong, extended, and spatially variable [OI] emission in the OMC2/3 region. HOPS 373 has one of the more well-developed outflows, has an  $\text{H}_2\text{O}$  maser (Haschick et al. 1983), and has the brightest line spectrum of all the PBRs.

Hollenbach & McKee (1989) predict strong far-infrared CO and [OI]  $63 \mu\text{m}$  emission for densities  $> 10^3 \text{ cm}^{-3}$  for fast, dissociative J-shocks with velocities  $> 30 \text{ km s}^{-1}$ . The

[OI] luminosity detected toward HOPS 373 is comparable to other protostars with similar luminosity (Green et al. 2013). While the tentative detections and non-detections toward the remaining PBRS do not point to anomalously weak [OI], we can confirm that the PBRS do not have exceptionally strong [OI] emission. Thus, we conclude that the outflows from the PBRS that give rise to the [OI] and high-J CO luminosities appear comparable in those tracers of other Class 0 protostars.

If PBRS are typical of the youngest protostars, early Class 0 protostars, then we posit that outflows may be very weak initially. At a minimum, the PACS [OI] and CO observations, in addition to CO ( $J = 1 \rightarrow 0$ ), demonstrate that the PBRS are not accompanied by significantly stronger outflows than typical Class 0 protostars. While the PBRS are inconsistent with the expected properties of first hydrostatic cores (FHSC) due to their luminosities and colors (ST13), the outflows predicted from FHSCs are quite weak  $< 15 \text{ km s}^{-1}$  (Tomida et al. 2013; Price et al. 2012). The outflows are expected to increase in velocity as the source evolves, though the simulations did not follow the longer term evolution. Such slow outflows from the PBRS would be consistent with them having recently transitioned out of a FHSC phase. If the outflow power is directly linked to the mass accretion rate, then the time in which protostars have very low outflow power is likely quite short  $< 10000 \text{ yr}$ , consistent with the apparent youth of the PBRS.

Alternatively, at  $63 \mu\text{m}$  the opacity from the infalling envelopes may be obscuring the [OI] emission. Following Kenyon et al. (1993), the optical depth through an envelope with a density profile consistent with free-fall ( $r^{-1.5}$ ) density profile (Ulrich 1976) is given by

$$\tau_\lambda = \frac{\kappa_\lambda \dot{M}}{2\pi(2GM_*)^{1/2}} r^{-1/2} \quad (1)$$

where  $\kappa_\lambda$  is the wavelength dependent dust opacity,  $G$  is the gravitational constant,  $\dot{M}$  is the mass infall rate,  $M_*$  is the protostar mass, and  $r$  is the inner radius for which the optical depth is being calculated.  $M_*$  is taken to be  $0.5 M_\odot$ , which is adopted to set the envelope density for a given infall rate; the absolute value for the mass is not important, only the envelope density. Under the assumption of free-fall collapse, the infall rate is directly proportional to the envelope density

$$\rho_{1000} = 2.378 \times 10^{-18} \left( \frac{\dot{M}_{env}}{10^{-5} M_\odot \text{yr}^{-1}} \right) \left( \frac{M_*}{0.5 M_\odot} \right) g \text{ cm}^{-3} \quad (2)$$

which is the volume density at a radius of 1000 AU, following the notation of Furlan et al. (2016). From spectral energy distribution model fitting to the Orion protostars (Furlan et al. 2016), the Class 0 protostars in Orion had median  $\rho_{1000}$  of  $5.9 \times 10^{-18} \text{ g cm}^{-3}$  with upper and lower quartiles of  $1.8 \times 10^{-18} \text{ g cm}^{-3}$  and  $1.8 \times 10^{-17} \text{ g cm}^{-3}$ . The PBRS considered here are

modeled by Furlan et al. (2016) to have a median  $\rho_{1000}$  of  $1.8 \times 10^{-17}$  g cm $^{-3}$ , and the SED fits tend to prefer densities of  $3 \times$  to  $10 \times$  higher than the typical and lowest density Class 0 protostars, respectively.

This difference in density translates to significantly more opacity at  $63 \mu\text{m}$  for the PBRs, a factor of  $4 \times$  to  $13 \times$  higher than the median Class 0 density and lower quartile; this results in a transmission of only 0.09 for a typical PBRs, versus 0.55 and 0.84 for the Class 0 median and lower Class 0 quartile, respectively. High opacity may be a particularly important consideration for 093005 which has a clear outflow in CO ( $J = 1 \rightarrow 0$ ), PACS CO, and H $_2$ O emission but without [OI] emission.

The high envelope opacities can also influence the CO rotation temperatures because the increasing optical depth at shorter wavelengths would cause the rotation temperatures to decrease due to flux attenuation of the line emission. To characterize the magnitude of this effect, we examined the difference in transmission for the PACS CO lines down to a radius of 1000 AU (where much of the PACS CO emission appears to be emitted, Green et al. 2013; Manoj et al. 2013). For typical Class 0 envelope densities ( $\rho_{1000} = 5.9 \times 10^{-18}$  g cm $^{-3}$ ), the typical density of the PBRs envelopes  $\rho_{1000} = 1.8 \times 10^{-17}$  g cm $^{-3}$ , and assuming dust opacities from Ossenkopf & Henning (1994, Table 1, column 5), we found that the  $3 \times$  higher envelope density could decrease the CO rotation temperatures by  $\sim 20$  K. Thus, the CO rotation temperatures of 220 K - 230 K would be higher if corrected for optical depth, making them even more consistent with the WISH/WILL/DIGIT/HOPS samples

## 5. Summary and Conclusions

We have presented an observational study of both the cold and warm/hot molecular gas in outflows from the youngest known protostars in the Orion molecular clouds, the PACS Bright Red Sources (PBRs). The cold gas was probed toward 14 out of 19 PBRs using observations of the CO ( $J = 1 \rightarrow 0$ ) transition from CARMA, and the warm/hot gas was examined for 8 out of the 19 PBRs using full spectral scans ( $55 \mu\text{m}$  to  $200 \mu\text{m}$ ) from the *Herschel* PACS far-infrared spectrometer. Finally, we also examined *Spitzer*  $4.5 \mu\text{m}$  imaging to look for evidence of both compact and extended outflow activity from both scattered light and shocked H $_2$  emission. The results from the follow-up work done in this study and Paper I demonstrate the critical need for complementary data in the determining the nature of protostellar sources that are otherwise only characterized by their SEDs. Our main conclusions are as follows.

1. We detect clear outflows toward 8 out of 14 PBRs (119019, 090003, 093005, 135003,

HOPS 373, 082012, and 019003) in the CO ( $J = 1 \rightarrow 0$ ) molecular transition. There is tentative evidence for outflows toward an additional three PBRs (HOPS 372, 302002, and 061012). We also detect outflows from two non-PBRs HOPS 223, a FU Ori-like outbursting protostar (Fischer et al. 2012) and HOPS 68 (Poteet et al. 2011); the HOPS 68 outflow also appears to be quadrupolar. No detectable outflow activity is found toward the PBRs 097002, 082005, 091015, and 091016 in CO ( $J = 1 \rightarrow 0$ ),  $4.5 \mu\text{m}$  emission, or far-infrared spectroscopy (only 091015 and 091016).

2. The outflows toward 090003 and 093005 are the most compact, subtending less than  $20''$  (8400 AU) in total extent, having dynamical ages  $\leq 2,500$  yr. These outflows are also found to have momenta, energies, and forces that are at the low end for Class 0 protostars. This observation, in addition to the lack of detectable outflows toward several other PBRs, leads us to suggest that outflows may start out weak in protostellar sources and become more energetic with time. These sources are also the only ones with flat visibility amplitudes to have detected outflows and we find a tentative tendency for the sources with flat visibility amplitudes in the 2.9 mm continuum (see Paper I) to either have no detected outflow activity or the most spatially compact outflows. This is further evidence for the sources with flat visibility amplitude being among the youngest protostars and the youngest PBRs.

3. The outflow from 082012 is extremely powerful, with red-shifted emission detected out to  $+40 \text{ km s}^{-1}$  from line center and extent greater than the CARMA primary beam. Its total energy is in excess of any individual outflow in the NGC 1333 star forming region (Plunkett et al. 2013) and comparable to some of the most powerful known outflows from Class 0 protostars (e.g., Hirano et al. 2010, L1448C).

4. We detect far-infrared CO emission lines toward 6 out of the 8 PBRs observed.  $\text{H}_2\text{O}$  lines are detected toward 5 out of 8 PBRs, and OH and [OI] are detected toward 1 PBR. The far-infrared CO,  $\text{H}_2\text{O}$ , and [OI] lines do not reveal outflows in the absence of outflow detections from other diagnostics. The CO luminosities and [OI] detections/upper limits are consistent with the results from larger samples of Class 0 protostars. However, the CO rotation temperatures tend to be lower than the typically observed 300 K CO rotation temperature for protostars; however, given the uncertainties the PBRs are consistent with the larger samples. Nevertheless, with a simple calculation of envelope opacity to a radius of 1000 AU, we find that the observed rotation temperatures of the PBRs could appear  $\sim 20$  K lower due to envelope opacity, given that the PBRs seem to have denser envelopes than typical Class 0 protostars.

We wish to thank the anonymous referee for excellent suggestions which have significantly improved the quality of the manuscript. The authors also wish to acknowledge fruitful discussions with M. Dunham, L. Kristensen, and J. Mottram regarding this work. J.J.T.

is currently supported by grant 639.041.439 from the Netherlands Organisation for Scientific Research (NWO). J.J.T acknowledges past support provided by NASA through Hubble Fellowship grant #HST-HF-51300.01-A awarded by the Space Telescope Science Institute, which is operated by the Association of Universities for Research in Astronomy, Inc., for NASA, under contract NAS 5-26555. The work of A.M.S. was supported by the Deutsche Forschungsgemeinschaft priority program 1573 ('Physics of the Interstellar Medium'). AK acknowledges support from the Foundation for Polish Science (FNP) and the Polish National Science Center grant 2013/11/N/ST9/00400. This work is based in part on observations made with Herschel, a European Space Agency Cornerstone Mission with significant participation by NASA. Support for this work was provided by NASA through an award issued by JPL/Caltech. We are very grateful to have had the opportunity to conduct these follow-up observations with the CARMA array in California. The discontinuation of support for this productive facility is a loss that will continue to be felt into the future. Support for CARMA construction was derived from the states of Illinois, California, and Maryland, the James S. McDonnell Foundation, the Gordon and Betty Moore Foundation, the Kenneth T. and Eileen L. Norris Foundation, the University of Chicago, the Associates of the California Institute of Technology, and the National Science Foundation. Ongoing CARMA development and operations are supported by the National Science Foundation under a cooperative agreement, and by the CARMA partner universities.

*Facilities:* CARMA, *Herschel*, *Spitzer*, Magellan

## A. Individual Sources

### A.1. HOPS 373

HOPS 373 is the close neighbor of 093005, located  $110''$  to the south. The dust continuum emission observed in D-configuration only showed some asymmetry and the combined D and C configuration data resolved a second component, separated by  $4''$  (Paper I). An outflow was previously detected in CO ( $J = 3 \rightarrow 2$ ) observations with the JCMT (Gibb & Little 2000) and an associated water maser by Haschick et al. (1983). Our observations of CO ( $J = 1 \rightarrow 0$ ) in Figure 6 show that the outflow has quite a wide angle and is extended beyond the primary beam. We also tentatively detected an outflow originating from the secondary source that has blue and red-shifted lobes opposite of the main outflow. The wide separation of the blue and red-shifted lobes indicates that the source is viewed at an inclination angle between  $50^\circ$  and  $80^\circ$ . There is higher-velocity redshifted emission observed away from the continuum source toward the edge of the primary beam.

The far-infrared line emission from this source is quite intense, detecting [OI], OH, CO, and H<sub>2</sub>O. The line emission from this source is the third brightest of all HOPS protostars and the only PBRs in our sample with confidently detected [OI] and OH emission.

### A.2. 093005

The reddest PBRs, 093005, is located at the intersection of three filaments and  $\sim 110''$  north of HOPS 373 (ST13). At wavelengths shorter than  $70 \mu\text{m}$ , 093005 was only detected in *Spitzer*  $3.6 \mu\text{m}$  and  $4.5 \mu\text{m}$  imaging (Figure 12a). The  $4.5 \mu\text{m}$  emission could be indicative of shocked H<sub>2</sub> emission and/or scattered light in an outflow cavity. Thus, a detection at  $4.5 \mu\text{m}$  is indicative of possible outflow activity toward this source. We clearly detect the CO outflow originating from 093005, as shown in Figure 1. The outflow appears compact with an offset between the red and blueshifted lobes of only  $\sim 3''$ . The position-velocity diagram of the outflow simply shows high-velocity emission offset from the protostar position, not the typical increasing velocity with distance as typical for many protostellar outflows (Arce et al. 2007). The features could result from a compact bow shock component as the outflow begins to break out from its envelope. However, the resolution of our observations was only  $\sim 3''$  (1200 AU), making clear determinations as to the nature of the high-velocity features difficult. The relative velocities of the red and blue-shifted lobes and their close spatial location indicate that the source is not oriented edge-on and is at an inclination angle of  $\sim 30^\circ$ . Compact bow-shocks viewed at an intermediate inclination could show observed morphology (Arce et al. 2007). Far-infrared CO and H<sub>2</sub>O line emission is also clearly detected toward this source.

### A.3. 090003

The PBRs 090003 (also called Orion B9 SMM 3; Miettinen et al. 2012) is located in a loose filamentary complex north of NGC 2024 with several protostars and starless cores over a 0.5 pc region (Miettinen et al. 2012). Much like 093005, the only detection shortward of  $24 \mu\text{m}$  for this source is at  $4.5 \mu\text{m}$ , where there is a small feature offset from the location of the protostar. This may be indicative of a knot of shocked H<sub>2</sub> emission (Miettinen et al. 2012; Stutz et al. 2013). The CO ( $J = 1 \rightarrow 0$ ) outflow from this source appears similar to that of 093005 and is indicative of  $\sim 30^\circ$  inclination, as shown in Figure 2; however, in contrast, there is a more spatially extended, low-velocity component. The high-velocities near the source and low velocities extended away from the source could be indicative of a wide-angle wind driving this outflow. Moreover, only  $\pm 1 \text{ km s}^{-1}$  around the systemic velocity is corrupted by

$^{12}\text{CO}$  emission from the cloud, so we are able to see lower-velocity features than in 093005. Miettinen et al. (2012) observed  $^{13}\text{CO}$  ( $J = 2 \rightarrow 1$ ) with APEX ( $\sim 30''$  resolution) and did not detect any indication of outflow emission from 090003, suggesting that the outflow is quite compact.

#### A.4. 082012 and HOPS 372

The outflow from 082012 is the brightest and one of the two most spatially extended outflows in the sample. Moreover, the outflow is visible over the largest velocity range (aside from HOPS 68) as shown by the 3 panels integrated at low, moderate, and high velocities in Figure 3. Sandell et al. (1999) previously reported single-dish CO ( $J = 3 \rightarrow 2$ ) and continuum maps at  $450 \mu\text{m}$  and  $850 \mu\text{m}$  toward this region. They resolved the dust emission around both protostars, and found a high-velocity outflow, consistent with our data, but mapped over a larger region,  $\pm 150''$  from the source.

The clear separation of the blue and redshifted lobes indicates an intermediate orientation of the source(s). The driving source of the collimated, high-velocity emission seems to be 082012; however, at lower velocities the red-shifted lobe extends back to HOPS 372 and there is blue-shifted emission that appears associated with HOPS 372 as well. Thus, the two outflows are nearly parallel and are perhaps interacting, but at a minimum their emission is clearly overlapping at lower velocities.

The highest observed outflow velocities toward 082012 are in excess of  $\pm 40 \text{ km s}^{-1}$  with multiple components being evident in the PV diagram and we can see the characteristic ‘Hubble-flow’ in the PV diagram. Furthermore, there are also red and blue-shifted CO emission clumps nearly orthogonal to the main outflow of 082012 which could be yet another outflow in the region. Furthermore, there are extended  $\text{H}_2$  knots along the position angle of the outflow from 082012 as shown in Figure 12a.

#### A.5. 135003

The PBRs 135003 is located in the OMC2/3 region of the Orion A cloud and located near OMC2-FIR6. The outflow from 135003 is well-collimated on the blue-shifted side, another source with a characteristic ‘Hubble-flow’ in the PV diagram, see Figure 5. The red-shifted, however, side does not appear as well-collimated near the source, but there is another red-shifted feature along the position angle, but outside the primary beam. An initial outflow detection was reported for this source by Shimajiri et al. (2009), consistent

with our measured position angle. Moreover, their single-dish CO ( $J = 3 \rightarrow 2$ ) data show that the outflow does extend outside our primary beam. The *Spitzer* 4.5  $\mu\text{m}$  map in Figure 12b shows a few knots of emission extending along the blue-shifted side of the outflow. H<sub>2</sub> imaging from Stanke et al. (2002) (SMZ 1-38) shows emission along both the northern (blue-shifted) and southern (red-shifted) sides of the outflow). This source also shows bright far-infrared CO and H<sub>2</sub>O features along its outflow, coinciding with the blue-shifted side of the outflow as shown in Figure 16a. We do not detect an outflow from its neighbor HOPS 59 within our sensitivity limits in low-J CO or PACS far-infrared lines.

### A.6. 019003

The PBRs source 019003 is also located in the OMC 2/3 region, northward of 135003. In Paper I, we detected 2 continuum sources toward the location of 019003 that were separated by  $\sim 10''$ ; the source associated with the PBRs is 019003-A and the other appears starless and is denoted 019003-B (Paper I). We detect an apparent outflow from 019003-A as shown in Figure 7 and the 4.5  $\mu\text{m}$  emission is also offset from the main outflow axis, similar to 090003, HOPS 373, and 302002. The surface brightness of the outflow is low, thus its detection is not as definitive as some of the others due to the crowded, confused region. Finally, there was no complementary detection in H<sub>2</sub> from Stanke et al. (2002).

### A.7. HOPS 68

The Class I protostar HOPS 68 is detected at the edge of the primary beam in the 019003 field. An outflow is well-detected from this source; the red-shifted lobe falls within the half-power point of the primary beam, while the blue-shifted lobe is located just outside the half-power point. The velocity distribution of the outflow indicates that it is located at an inclination angle of  $50^\circ$  from comparison to the models of Cabrit & Bertout (1986). An intermediate outflow inclination was necessary for a model by (Poteet et al. 2011) to explain the relatively flat SED between 3.6  $\mu\text{m}$  to 24  $\mu\text{m}$ , deep silicate absorption feature, and crystalline silicate features observed with *Spitzer*; the crystalline dust is postulated to have been formed by shocks in the outflow cavity walls. Furthermore, there are apparently two outflows from this source, a lower velocity outflow that is more east-west in orientation (PA  $\sim 230^\circ$ ), but at higher velocities there is an apparent shift and the outflow is more north-south in orientation (PA  $\sim 160^\circ$ ). However, the blue-shifted side has both components out to the highest velocities we can measure. We overlay the integrated intensity maps of the high-velocity emission on a Ks-band image in Figure 8, and there are apparent outflow fea-

tures associated with both the northwest-southeast component and the northeast-southwest component. H<sub>2</sub> imaging by Stanke et al. (2002) confirms that these knots are H<sub>2</sub> emission (SMZ 1-28) and they also suggested that the driving source was FIR2 from Chini et al. (1997) (coincident with HOPS 68).

### A.8. 302002

The PBRs 302002 is located at the end of an isolated filamentary structure in NGC 2068, it is located  $\sim 20''$  to the south of a Class I source (HOPS 331). 302002 is undetected at 24  $\mu\text{m}$  but does seem to have emission at 4.5  $\mu\text{m}$ , indicative of an outflow cavity or shocked H<sub>2</sub> emission in the outflow, see Figure 12b. We show in Figure 9 that there appears to be outflow emission associated with this source; however, the blue and red-shifted emission are not located on the same position angle from the source. The blue-shifted emission is narrow and extends out to the edge of the primary beam. The red-shifted emission on the other hand is quite compact and located in a single clump offset west of the protostar. The CO outflow direction is marginally consistent with the apparent orientation in the 4.5  $\mu\text{m}$  imaging. The poorly detected outflow and low-velocity of the emission may indicate that this source is close to edge-on. From the comparison to Cabrit & Bertout (1986), the outflow could be between 50° and 80° but likely closer to 80°.

### A.9. 061012 and HOPS 223

The PBRs 061012 is located very near the outbursting protostar V2775 Ori (HOPS 223) in the L1641 region (Fischer et al. 2012). The outflow toward 061012 cannot be unambiguously disentangled from that of HOPS 223 in the integrated velocity map shown in Figure 10. However, looking at the PV diagram of the <sup>12</sup>CO emission centered on the continuum source of 061012, we do see evidence of higher velocity emission near the protostar. The position angle of the outflow is estimated from the resolved 4.5  $\mu\text{m}$  emission shown in Stutz et al. (2013) and there are H<sub>2</sub> emission knots at 4.5  $\mu\text{m}$  extending almost 0.3 pc from the source (Figure 12b). Thus, we may be detecting an inner, compact outflow toward this protostar. The outflow from HOPS 223 appears quite wide, bright and clumpy in the integrated intensity map and PV diagram in Figure 10. The clumpiness could in part result from spatial filtering and that the source is toward the edge of the primary beam with increased noise. However, episodic mass ejection episodes could contribute to the clumpiness of the outflow emission, which has been seen in outflow data toward HH 46/47 (Arce et al. 2013).

#### A.10. 091015 and 091016

The PBRS 091015 and 091016 are close neighbors in NGC 2068, 091016 being  $\sim 40''$  east of 091015; these sources are completely undetected at wavelengths shortward of  $70 \mu\text{m}$ . We do not detect evidence of outflow emission from these sources at any wavelength. Given that a substantial amount of cloud emission is resolved-out at line center, there could be lower-velocity outflow emission associated with these sources that we simply cannot detect with the current data. Observations of higher-excitation CO transitions at higher resolution may better distinguish potential outflow emission from these sources. However, we also did not detect any far-infrared line emission from these sources, a further indication that any outflows from these sources may be weak, or completely buried within their the optically thick envelopes.

#### A.11. 082005

The PBRS 082005 is located about  $4'$  south of 082012, and these sources are connected by a filamentary structure detected at  $870 \mu\text{m}$  and  $160 \mu\text{m}$ . This source is also undetected at wavelengths shorter than  $70 \mu\text{m}$ . No CO outflow emission was detected in our CARMA observations toward this source and we see no evidence for outflow emission from the *Spitzer*  $4.5 \mu\text{m}$  maps in Figure 12c.

#### A.12. 097002

The PBRS 097002 is found near a bright  $4.5 \mu\text{m}$  and  $24 \mu\text{m}$  source as seen in *Spitzer* data shown by Stutz et al. (2013); however, this short wavelength emission is not from 097002, which is only detected at  $70 \mu\text{m}$  and longer wavelengths. We do not detect an outflow from this source in our CO ( $J = 1 \rightarrow 0$ ) maps, but the continuum is quite bright (Paper I). However, there is some emission detected near line-center at the source position.

#### A.13. 119019

The outflow toward 119019 has complete spatial overlap between the red and blue-shifted emission meaning that this source is viewed almost exactly edge-on. This source was also one of the fainter continuum sources detected in (Paper I). Therefore, unlike the rest of the sample, this source may only have been identified as a PBRS due to an edge-on

orientation. The outflow extends outside the CARMA primary beam and the velocity width of the outflow is quite narrow, only  $\pm 3 \text{ km s}^{-1}$ ; however, the outflow may have greater speeds given that we are viewing it in the plane of the sky. Some diffuse emission is detected at  $4.5 \mu\text{m}$  near the protostar location and along the outflow in figure 12b; Davis et al. (2009) also detects  $\text{H}_2$  knots that appear to be part of this outflow (DFS 136). This source also has the faintest far-infrared line emission for which we have a confident detection.

## REFERENCES

- Ali, B., Tobin, J. J., Fischer, W. J., et al. 2010, *A&A*, 518, L119
- Andre, P., Ward-Thompson, D., & Barsony, M. 1993, *ApJ*, 406, 122
- Arce, H. G., Mardones, D., Corder, S. A., et al. 2013, *ApJ*, 774, 39
- Arce, H. G., & Sargent, A. I. 2006, *ApJ*, 646, 1070
- Arce, H. G., Shepherd, D., Gueth, F., et al. 2007, *Protostars and Planets V*, 245
- Bally, J., Reipurth, B., Lada, C. J., & Billawala, Y. 1999, *AJ*, 117, 410
- Bontemps, S., Andre, P., Terebey, S., & Cabrit, S. 1996, *A&A*, 311, 858
- Cabrit, S., & Bertout, C. 1986, *ApJ*, 307, 313
- Cassen, P., & Moosman, A. 1981, *Icarus*, 48, 353
- Chen, X., Arce, H. G., Zhang, Q., et al. 2010, *ApJ*, 715, 1344
- Chini, R., Reipurth, B., Ward-Thompson, D., et al. 1997, *ApJ*, 474, L135
- Davis, C. J., Froebrich, D., Stanke, T., et al. 2009, *A&A*, 496, 153
- Dunham, M. M., Chen, X., Arce, H. G., et al. 2011, *ApJ*, 742, 1
- Dunham, M. M., Evans, II, N. J., Bourke, T. L., et al. 2006, *ApJ*, 651, 945
- Dunham, M. M., Stutz, A. M., Allen, L. E., et al. 2014, *Protostars and Planets VI*, 195
- Enoch, M. L., Lee, J.-E., Harvey, P., Dunham, M. M., & Schnee, S. 2010, *ApJ*, 722, L33
- Fischer, W. J., Megeath, S. T., Ali, B., et al. 2010, *A&A*, 518, L122
- Fischer, W. J., Megeath, S. T., Tobin, J. J., et al. 2012, *ApJ*, 756, 99
- Flower, D. R., & Pineau Des Forêts, G. 2010, *MNRAS*, 406, 1745

- Flower, D. R., & Pineau des Forêts, G. 2015, *A&A*, 578, A63
- Frank, A., Ray, T. P., Cabrit, S., et al. 2014, *Protostars and Planets VI*, 451
- Frerking, M. A., Langer, W. D., & Wilson, R. W. 1982, *ApJ*, 262, 590
- Furlan, E., Fischer, W. J., Ali, B., et al. 2016, *ApJS*, 224, 5
- Gibb, A. G., & Little, L. T. 2000, *MNRAS*, 313, 663
- Green, J. D., Evans, II, N. J., Jørgensen, J. K., et al. 2013, *ApJ*, 770, 123
- Haschick, A. D., Moran, J. M., Rodriguez, L. F., & Ho, P. T. P. 1983, *ApJ*, 265, 281
- Hirano, N., Ho, P. T. P., Liu, S.-Y., et al. 2010, *ApJ*, 717, 58
- Hollenbach, D. 1985, *Icarus*, 61, 36
- Hollenbach, D., & McKee, C. F. 1989, *ApJ*, 342, 306
- Karska, A., Herczeg, G. J., van Dishoeck, E. F., et al. 2013, *A&A*, 552, A141
- Karska, A., Kristensen, L. E., van Dishoeck, E. F., et al. 2014, *A&A*, 572, A9
- Kaufman, M. J., & Neufeld, D. A. 1996, *ApJ*, 456, 611
- Kenyon, S. J., Calvet, N., & Hartmann, L. 1993, *ApJ*, 414, 676
- Langer, W. D., & Penzias, A. A. 1993, *ApJ*, 408, 539
- Larson, R. B. 1969, *MNRAS*, 145, 271
- Lee, C., Hirano, N., Palau, A., et al. 2009, *ApJ*, 699, 1584
- Lee, C.-F., Ho, P. T. P., Bourke, T. L., et al. 2008, *ApJ*, 685, 1026
- Lee, C.-F., Mundy, L. G., Reipurth, B., Ostriker, E. C., & Stone, J. M. 2000, *ApJ*, 542, 925
- Li, Z.-Y., Banerjee, R., Pudritz, R. E., et al. 2014, *Protostars and Planets VI*, 173
- Li, Z.-Y., Krasnopolsky, R., & Shang, H. 2013, *ApJ*, 774, 82
- Looney, L. W., Mundy, L. G., & Welch, W. J. 2000, *ApJ*, 529, 477
- Manoj, P., Watson, D. M., Neufeld, D. A., et al. 2013, *ApJ*, 763, 83
- Martini, P., Persson, S. E., Murphy, D. C., et al. 2004, in *Society of Photo-Optical Instrumentation Engineers (SPIE) Conference Series*, Vol. 5492, *Ground-based Instrumentation for Astronomy*, ed. A. F. M. Moorwood & M. Iye, 1653–1660

- Megeath, S. T., Gutermuth, R., Muzerolle, J., et al. 2012, *AJ*, 144, 192
- Miettinen, O., Harju, J., Haikala, L. K., & Juvela, M. 2012, *A&A*, 538, A137
- Myers, P. C., & Ladd, E. F. 1993, *ApJ*, 413, L47
- Nisini, B., Santangelo, G., Giannini, T., et al. 2015, *ApJ*, 801, 121
- Offner, S. S. R., & Arce, H. G. 2014, *ApJ*, 784, 61
- Ossenkopf, V., & Henning, T. 1994, *A&A*, 291, 943
- Pilbratt, G. L., Riedinger, J. R., Passvogel, T., et al. 2010, *A&A*, 518, L1
- Pineda, J. E., Arce, H. G., Schnee, S., et al. 2011, *ApJ*, 743, 201
- Plunkett, A. L., Arce, H. G., Corder, S. A., et al. 2013, *ApJ*, 774, 22
- Poglitsch, A., Waelkens, C., Geis, N., et al. 2010, *A&A*, 518, L2
- Poteet, C. A., Megeath, S. T., Watson, D. M., et al. 2011, *ApJ*, 733, L32
- Price, D. J., Tricco, T. S., & Bate, M. R. 2012, *MNRAS*, 423, L45
- Rebull, L. M., Stapelfeldt, K. R., Evans, II, N. J., et al. 2007, *ApJS*, 171, 447
- Reipurth, B., Aspin, C., Bally, J., Tobin, J. J., & Walawender, J. 2010, *AJ*, 140, 699
- Reipurth, B., Hartigan, P., Heathcote, S., Morse, J. A., & Bally, J. 1997, *AJ*, 114, 757
- Sadavoy, S. I., Di Francesco, J., André, P., et al. 2014, *ApJ*, 787, L18
- Sandell, G., Avery, L. W., Baas, F., et al. 1999, *ApJ*, 519, 236
- Santiago-García, J., Tafalla, M., Johnstone, D., & Bachiller, R. 2009, *A&A*, 495, 169
- Sault, R. J., Teuben, P. J., & Wright, M. C. H. 1995, in *Astronomical Society of the Pacific Conference Series, Vol. 77, Astronomical Data Analysis Software and Systems IV*, ed. R. A. Shaw, H. E. Payne, & J. J. E. Hayes, 433–+
- Schnee, S., Di Francesco, J., Enoch, M., et al. 2012, *ApJ*, 745, 18
- Shimajiri, Y., Takahashi, S., Takakuwa, S., Saito, M., & Kawabe, R. 2009, *PASJ*, 61, 1055
- Shu, F. H. 1977, *ApJ*, 214, 488
- Snell, R. L., Loren, R. B., & Plambeck, R. L. 1980, *ApJ*, 239, L17
- Stanke, T., McCaughrean, M. J., & Zinnecker, H. 2002, *A&A*, 392, 239

- Stanke, T., Stutz, A. M., Tobin, J. J., et al. 2010, *A&A*, 518, L94
- Stutz, A. M., Tobin, J. J., Stanke, T., et al. 2013, *ApJ*, 767, 36
- Takahashi, S., Saigo, K., Ho, P. T. P., & Tomida, K. 2012, *ApJ*, 752, 10
- Terebey, S., Shu, F. H., & Cassen, P. 1984, *ApJ*, 286, 529
- Tobin, J. J., Hartmann, L., Looney, L. W., & Chiang, H.-F. 2010, *ApJ*, 712, 1010
- Tobin, J. J., Looney, L. W., Mundy, L. G., Kwon, W., & Hamidouche, M. 2007, *ApJ*, 659, 1404
- Tobin, J. J., Hartmann, L., Chiang, H.-F., et al. 2011, *ApJ*, 740, 45
- Tobin, J. J., Stutz, A. M., Megeath, S. T., et al. 2015, *ApJ*, 798, 128
- Tomida, K., Tomisaka, K., Matsumoto, T., et al. 2013, *ApJ*, 763, 6
- Ulrich, R. K. 1976, *ApJ*, 210, 377
- van der Marel, N., Kristensen, L. E., Visser, R., et al. 2013, *A&A*, 556, A76
- van Kempen, T. A., Kristensen, L. E., Herczeg, G. J., et al. 2010, *A&A*, 518, L121
- Whitney, B. A., Wood, K., Bjorkman, J. E., & Wolff, M. J. 2003, *ApJ*, 591, 1049
- Yıldız, U. A., Kristensen, L. E., van Dishoeck, E. F., et al. 2015, *A&A*, 576, A109
- Young, C. H., Jørgensen, J. K., Shirley, Y. L., et al. 2004, *ApJS*, 154, 396

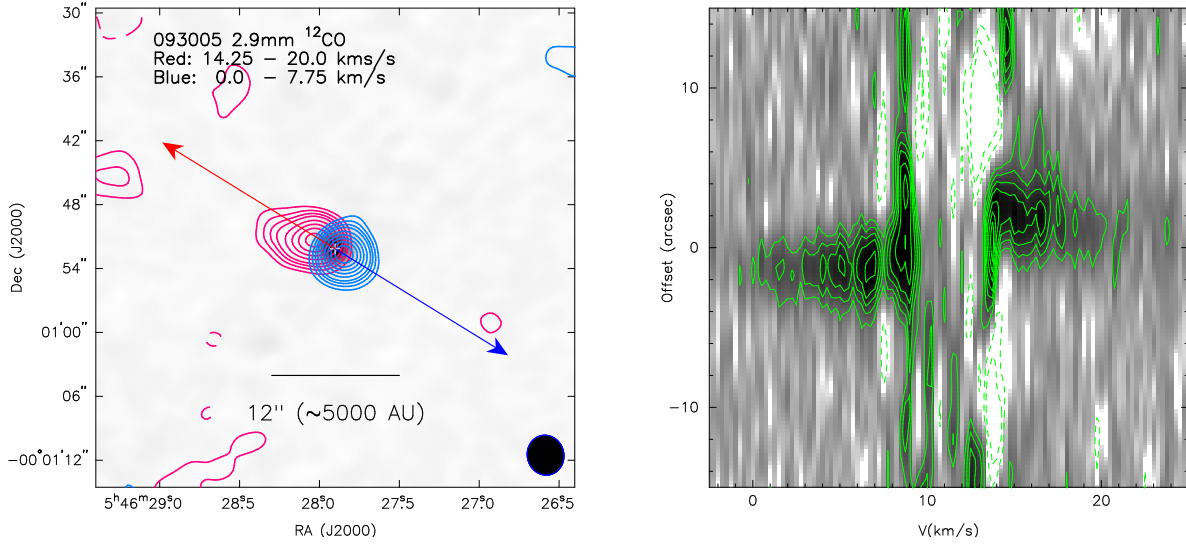


Fig. 1.— PBRs 093005 – Red and blue-shifted  $^{12}\text{CO}$  ( $J = 1 \rightarrow 0$ ) integrated intensity contours are overlaid on the 2.9 mm continuum image from combined D and C configuration data. The compact outflow is centered on the continuum source; the position velocity plot on the right shows the velocity distribution of the  $^{12}\text{CO}$  emission along the red and blue vectors marking the outflow axis. The cross marks the position of the protostar inferred from the 2.9 mm continuum. The PV plot shows that the emission is compact and confined to regions near the source. The contours in the integrated intensity plot are  $[\pm 6, 9, 12, 15, 20, 30, 40, 50, 60] \times \sigma$  for the blue and the red;  $\sigma_{red} = 0.84$  K and  $\sigma_{blue} = 0.72$  K. The PV plot contours are  $[-6, -3, 3, 5, 7, 9, 12, 15, 18, 21, 24, 27, 30] \times \sigma$  and  $\sigma = 0.65$  K.

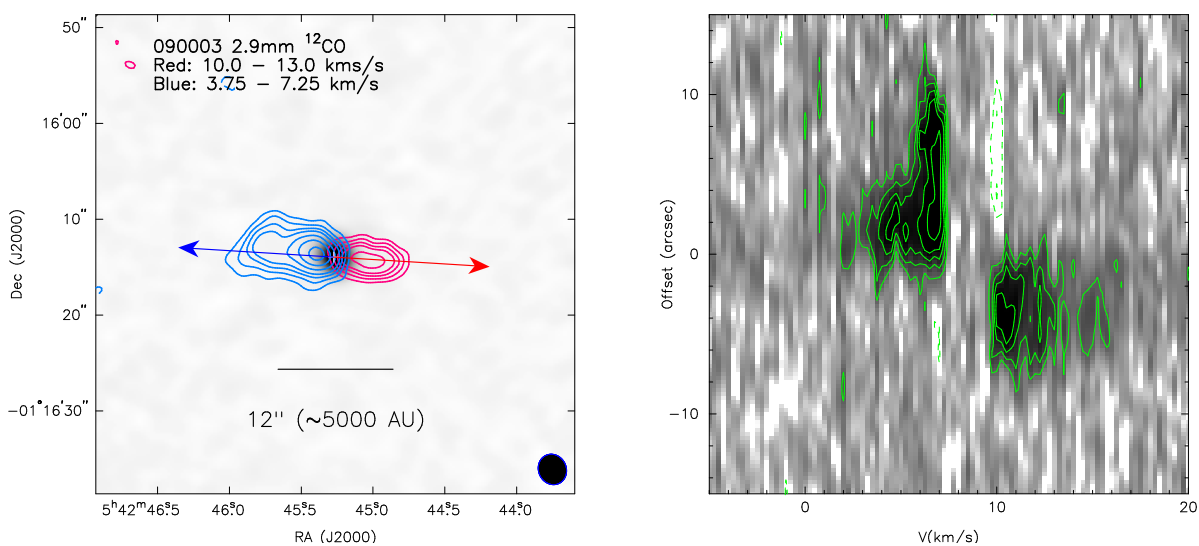


Fig. 2.— PBRs 090003 – Same as Figure 1; the outflow toward this source is similar to 093005 in that it is compact and collimated. But, there is a bit more spatial separation between the high-velocity components. The contours in the integrated intensity plot are  $[\pm 6, 9, 12, 15, 20, 25, 30, 35, 40, 45, 50] \times \sigma$  for the blue and the red;  $\sigma_{red} = 0.58$  K and  $\sigma_{blue} = 0.66$  K. The PV plot contours are  $[-6, -3, 3, 5, 7, 9, 12, 15, 18, 21, 24, 27, 30] \times \sigma$  and  $\sigma = 0.4$  K.

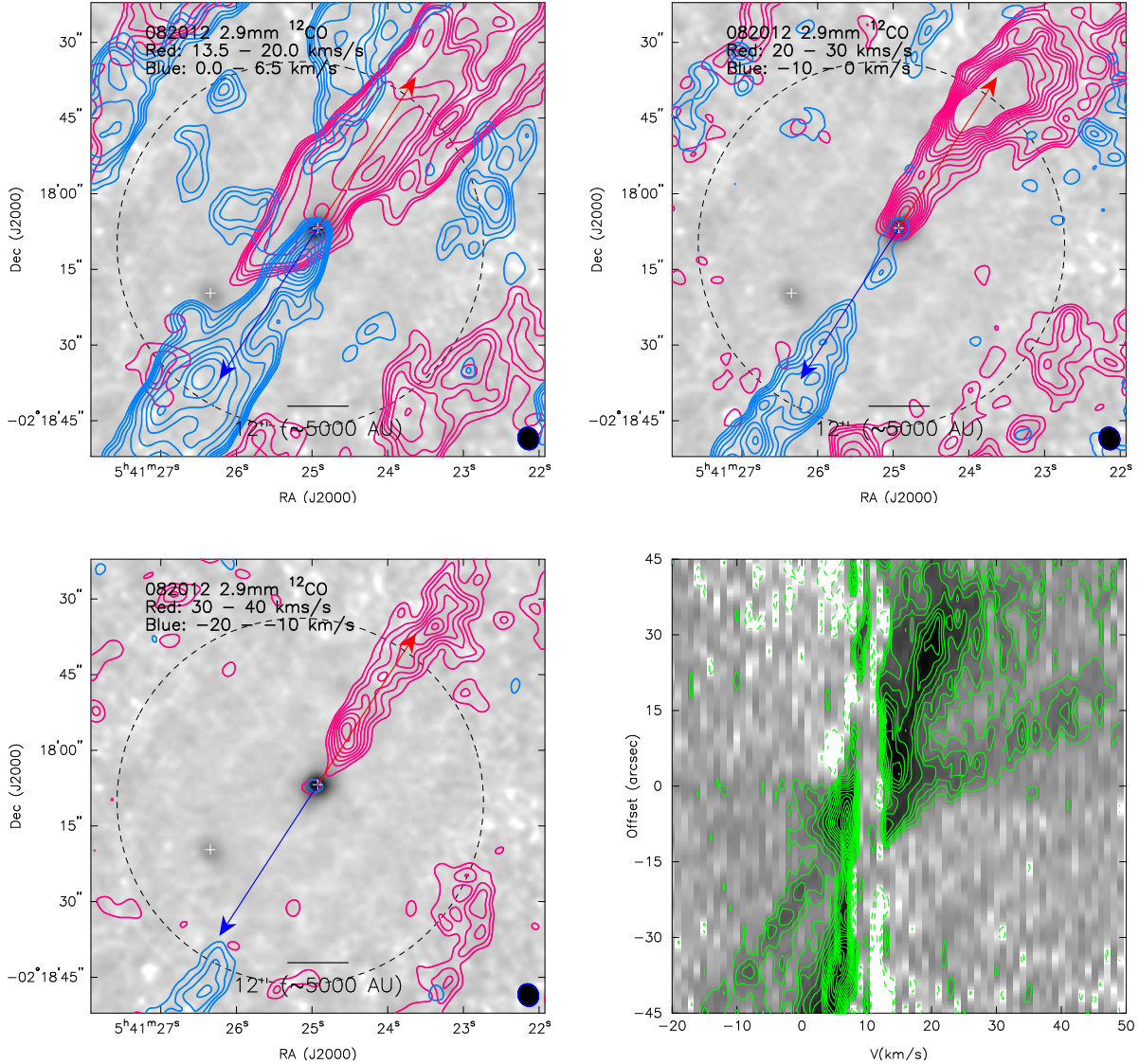


Fig. 3.— PBRs 082012 – Same as Figure 1, showing both 082012 (center cross) and HOPS 372 (southeast cross). The outflow from 082012 is a very strong, collimated outflow that is extended to a large distance away from the protostar. We show three plots at low (0 - 20 km s<sup>-1</sup>), moderate (20 - 30 km s<sup>-1</sup>; -10 - 0 km s<sup>-1</sup>), and high (30 - 40 km s<sup>-1</sup>; -20 - -10 km s<sup>-1</sup>). The blue-shifted side disappears at velocities higher than -10 km s<sup>-1</sup> and the outflow becomes more narrow and jet like at the higher velocities. The low velocity emission appears to trace the combination of an outflow from HOPS 372 and 082012, with 082012 being dominant. Then at higher velocities, the 082012 outflow is most apparent and HOPS 372 does not seem to contribute. The PV plot clearly shows the high and low velocity components of the outflow. The contours in the low velocity plot are [ $\pm 6, 9, 12, 15, 20, 30, 40, 50, 60, 70$ ]  $\times \sigma$  for the blue and the red;  $\sigma_{red} = 1.27$  K and  $\sigma_{blue} = 1.27$  K. For the remaining plots the contours are [ $-6, -4, 4, 6, 8, \dots, 24$ ]  $\sigma$ ;  $\sigma_{red}$  and  $\sigma_{blue} = 1.56$  K. The PV plot contours are [ $-6, -3, 3, 5, 7, 9, 12, 15, 18, 21, 24, 27, 30, 35$ ]  $\times \sigma$  and  $\sigma = 0.35$  K. The half-power point of the primary beam is plotted as the dashed circle

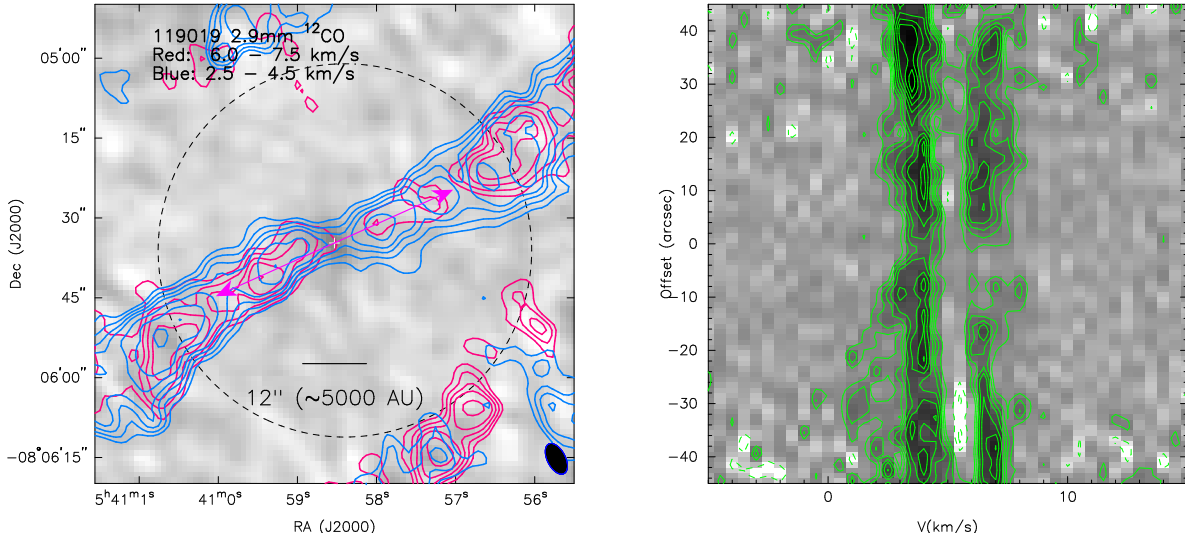


Fig. 4.— PBRs 119019 – Same as Figure 1, but for D-configuration only. The outflow toward 119019 appears nearly in the plane of the sky, this is because the outflow is very extended and the red and blue-shifted emission have spatial overlap in all locations with detected emission. The full extent goes beyond the CARMA primary beam (dashed circle). The PV diagram further shows the low velocities and overlap of red and blue-shifted emission along the outflow. The contours in the integrated intensity plot are  $[\pm 6, 9, 12, 15, 20, 25, 30, 35, 40, 45, 50, 60, 70] \times \sigma$  for the blue and the red;  $\sigma_{red} = 0.48$  K and  $\sigma_{blue} = 0.54$  K. The PV plot contours are  $[-6, -3, 3, 5, 7, 9, 12, 15, 18, 21, 24, 27, 30] \times \sigma$  and  $\sigma = 0.4$  K.

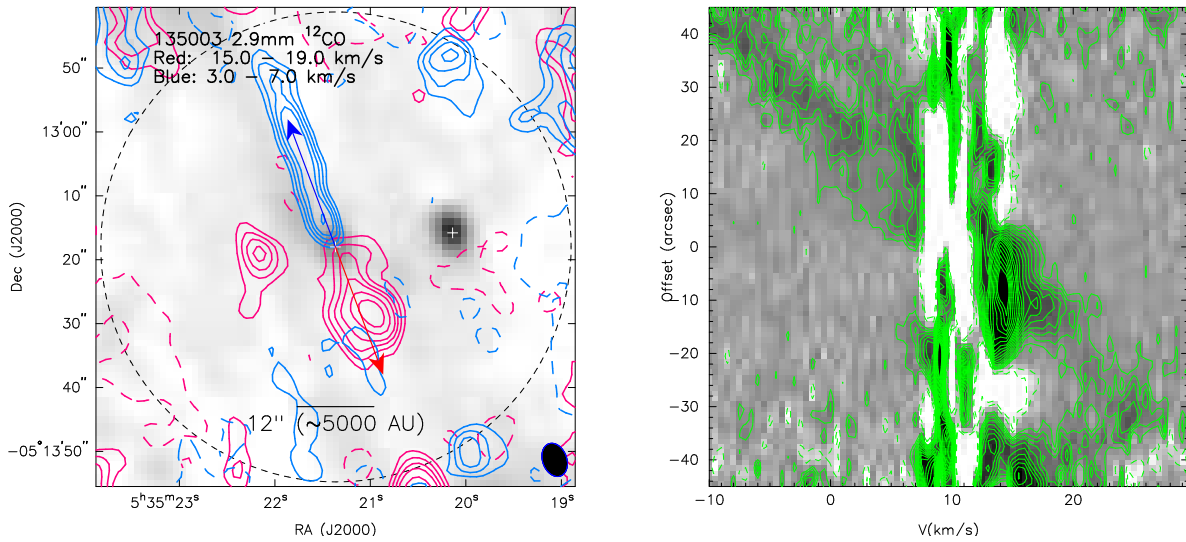


Fig. 5.— PBRS 135003— Same as Figure 1, but for D-configuration only. The continuum peak of PBRS 135003 is in the center of the image and marked with a cross. HOPS 59 is also present in this field and marked with the cross in the western part of the image. the contours in the integrated intensity map start at  $\pm 10\sigma$  and increase in  $5\sigma$  intervals for the blue and the red-shifted contours start are  $[-6, 6, 9, 12, 15, 20, \dots, 60] \times \sigma$ ;  $\sigma_{red}, \sigma_{blue} = 0.86$  K. The PV plot contours are  $[-6, -3, 3, 5, 7, 9, 12, 15, 18, 21, 24, 27, 30, 35, \dots, 60] \times \sigma$  and  $\sigma = 0.75$  K. The half-power point of the primary beam is plotted as the dashed circle.

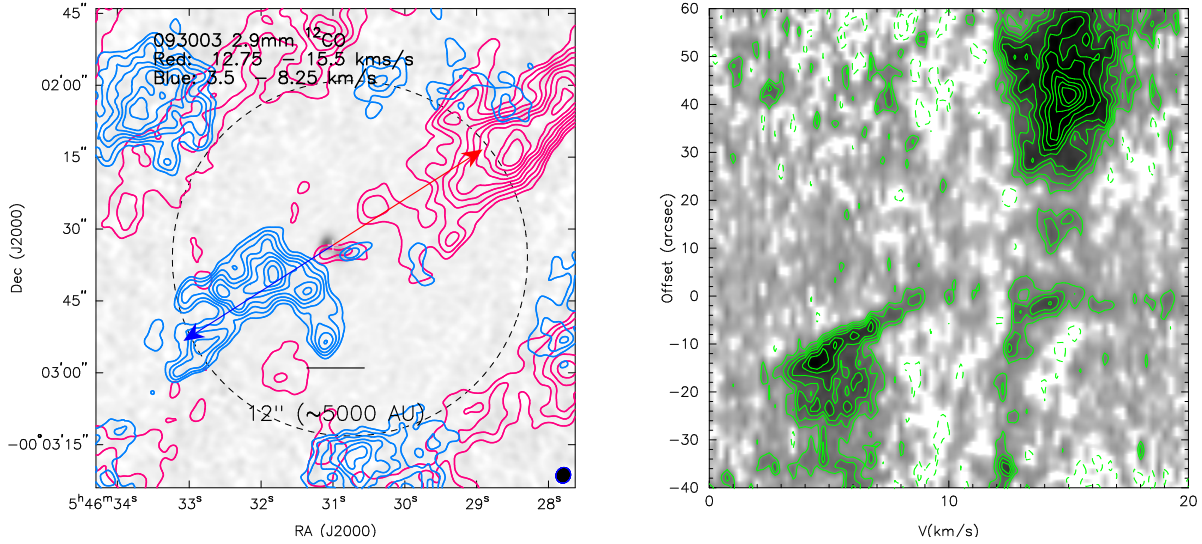


Fig. 6.— PBRs HOPS 373 – Same as Figure 1, the outflow toward HOPS 373 is wide and was known to have a large outflow from single-dish studies (Gibb & Little 2000). Very near the protostar there is compact blue-shifted and red-shifted emission in the opposite directions as compared to the larger outflow; this may be a second outflow from the binary source. The PV plot shows the blue-shifted component on either side of the protostar and the red-shifted component is evident at a large distance from the protostar; note that most of the red-shifted lobe is outside the primary beam of CARMA. The contours in the line map start at  $\pm 10\sigma$  and increase in  $5\sigma$  intervals for the blue and the red-shifted contours start at  $\pm 20\sigma$  and increase in  $10\sigma$ ;  $\sigma_{red} = 0.93$  K and  $\sigma_{blue} = 1.21$  K. The PV plot contours are  $[-6, -3, 3, 5, 7, 9, 12, 15, 18, 21, 24, 27, 30, 35, \dots, 60] \times \sigma$  and  $\sigma = 0.75$  K. The half-power point of the primary beam is plotted as the dashed circle.

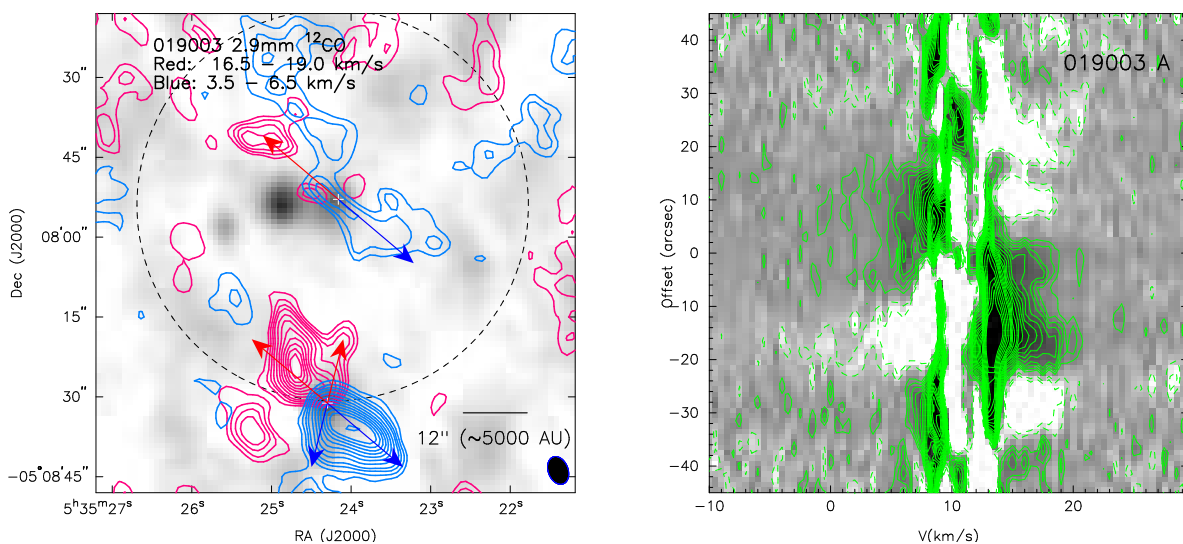


Fig. 7.— PBRs 019003— Same as Figure 1, with data from D-configuration only. HOPS 68 is located in the southern part of the map and is shown in more detail in Figure 8. The contours in the line map start at  $\pm 10\sigma$  and increase in  $5\sigma$  intervals for the blue and the red-shifted contours start at  $\pm 20\sigma$  and increase in  $10\sigma$ ;  $\sigma_{red} = 1.6$  K and  $\sigma_{blue} = 1.56$  K. The PV plot contours are  $[-6, -3, 3, 5, 7, 9, 12, 15, 18, 21, 24, 27, 30, 35, \dots, 60] \times \sigma$  and  $\sigma = 0.75$  K. The half-power point of the primary beam is plotted as the dashed circle.

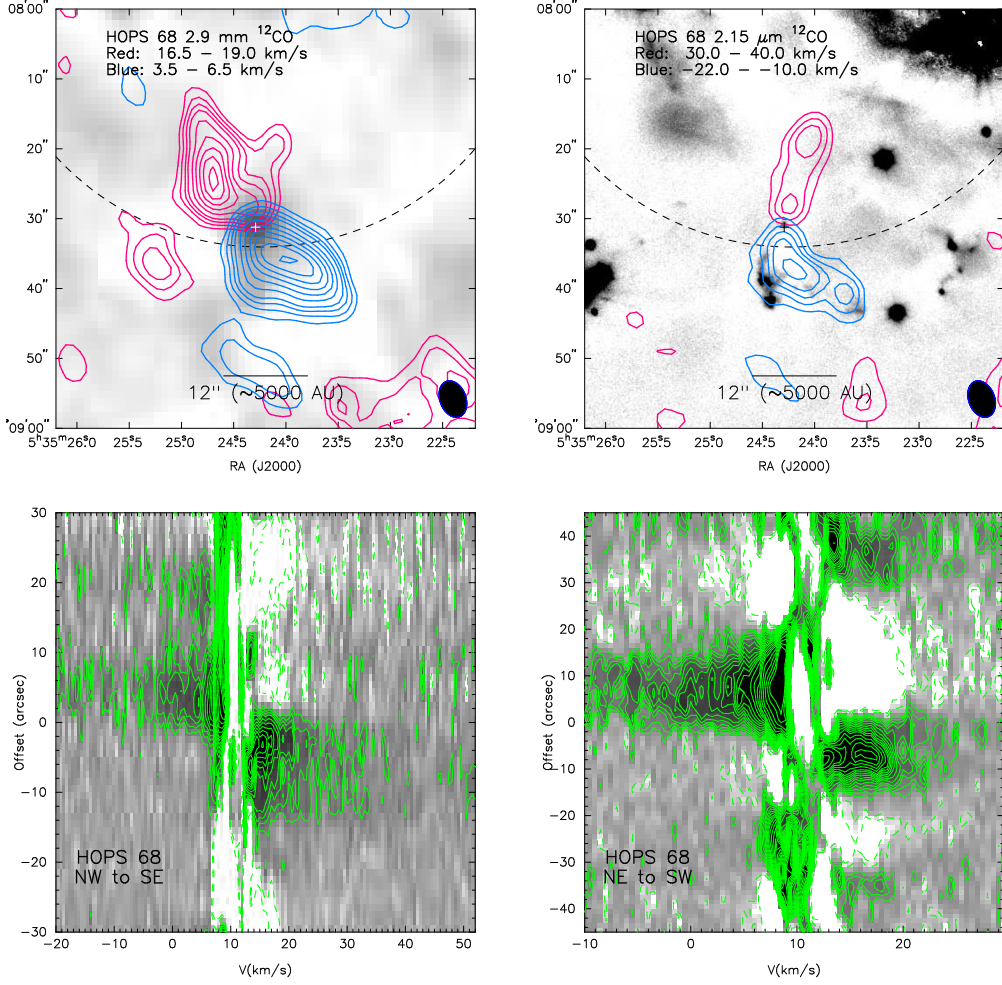


Fig. 8.— HOPS 68— Zoom in on the HOPS 68 outflow(s). We show plots of the low velocity CO contours ( $3.5 - 6.5 \text{ km s}^{-1}$ ;  $16.5 - 19.5 \text{ km s}^{-1}$ ) overlaid on the 2.9 mm continuum image and we overlaid the high velocity CO ( $30 - 40 \text{ km s}^{-1}$ ;  $-22 - -10 \text{ km s}^{-1}$ ) contours on the Ks-band ( $2.15 \mu\text{m}$ ) image from Magellan PANIC. Between the high and low velocity ranges, the apparent position angle of the outflow changes from about  $225^\circ$  to  $170^\circ$ . The contours in all plots are plot are  $[\pm 6, 9, 12, 15, 20, 30, 40, 50, 60, 70] \times \sigma$ ;  $\sigma_{red} = 1.1 \text{ K}$  and  $1.39 \text{ K}$  for the low and high velocities. For the blue contours,  $\sigma_{blue} = 1.0 \text{ K}$  and  $1.55 \text{ K}$  for the low and high velocities. The PV plot contours are  $[-6, -3, 3, 5, 7, 9, 12, 15, 18, 21, 24, 27, 30, 35, \dots, 60] \times \sigma$  and  $\sigma = 0.45 \text{ K}$ . The half-power point of the primary beam is plotted as the dashed arc.

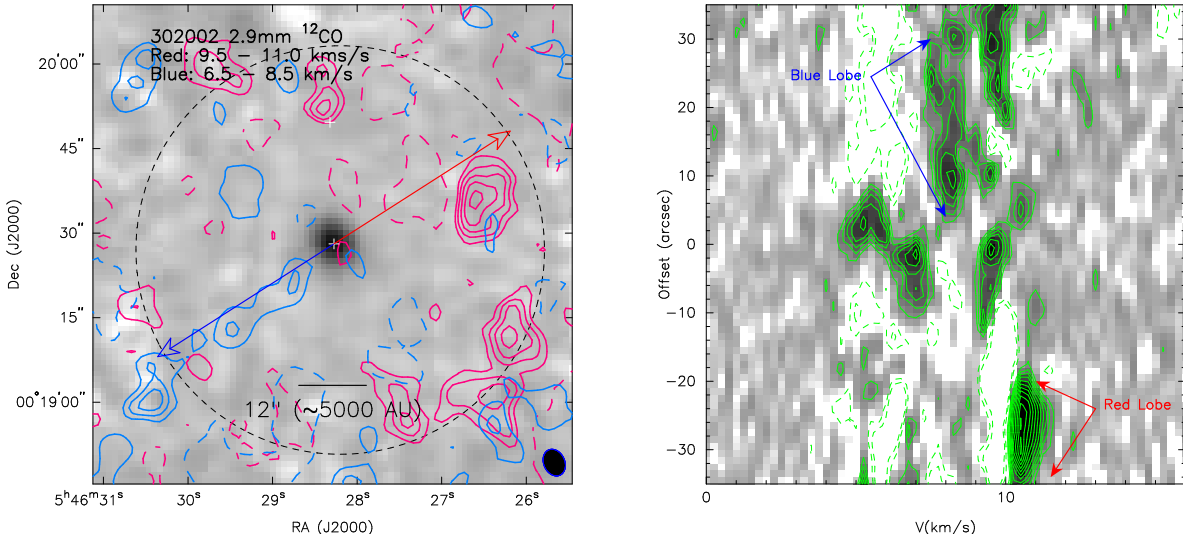


Fig. 9.— PBRs 302002 – Same as Figure 1, but with D-configuration only. This source has some evidence of an outflow, however it is at low signal to noise and the blue and red-shifted lobes are not exactly in a linear configuration. The PV plot shows that the outflow emission has quite low intensity and the plot is also more complex than others because there appears to be a foreground cloud at  $\sim 6 \text{ km s}^{-1}$  which results in more resolved-out flux. We have labeled the blue and red-shifted lobes that are shown in the integrated intensity plot. North of 302002, HOPS 331 is not detected in the 2.9 mm continuum, but is marked with a cross. There is red-shifted CO emission associated with HOPS 331, appearing to be an outflow from this source. The contours start at  $\pm 10\sigma$  and increase in  $5\sigma$  intervals;  $\sigma_{red} = 0.41 \text{ K}$  and  $\sigma_{blue} = 0.46 \text{ K}$ . The half-power point of the primary beam is plotted as the dashed circle.

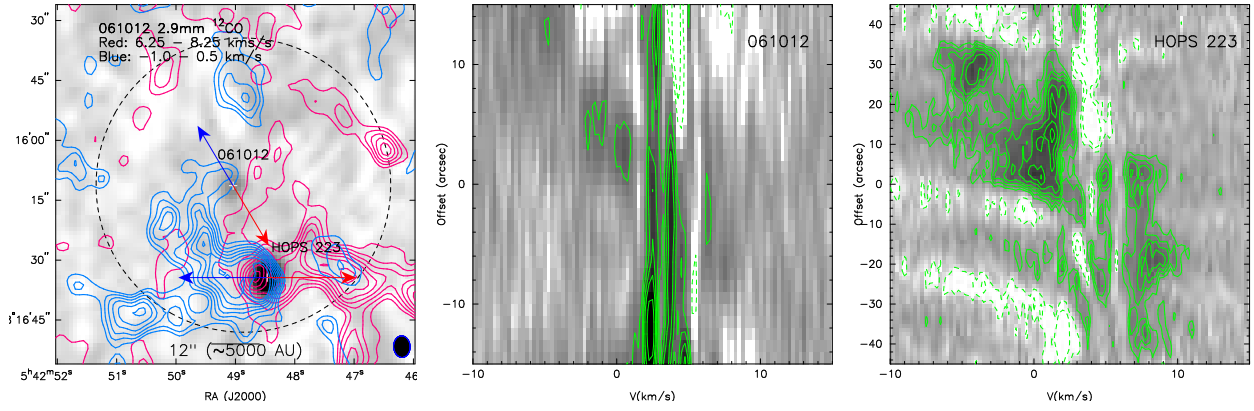


Fig. 10.— PBRs 061012 and HOPS 223 – Same as Figure 1, but for D-configuration data only. There is not a clear outflow detection from 061012; however, it is strongly confused with the outflow being driven by HOPS 223 and may need higher resolution to disentangle. The PV plot shows that there is a blue-shifted feature that is along a possible outflow axis for 061012. The outflow of HOPS 223 looks quite complex in the PV diagram with multiple velocity components; note that spatial filtering may be causing this outflow to appear more complex than it truly is. The contours in the line map start at  $10\sigma$  and increase in  $5\sigma$  intervals for the blue and the red-shifted contours start at  $10\sigma$  and increase in  $5\sigma$ ;  $\sigma_{red} = 0.44$  K and  $\sigma_{blue} = 0.46$  K. Negative contours are not drawn for clarity. The PV plot contours are  $[-6, -3, 3, 5, 7, 9, 12, 15, 18, 21, 24, 27, 30] \times \sigma$  and  $\sigma = 0.65$  K. The half-power point of the primary beam is plotted as the dashed circle.

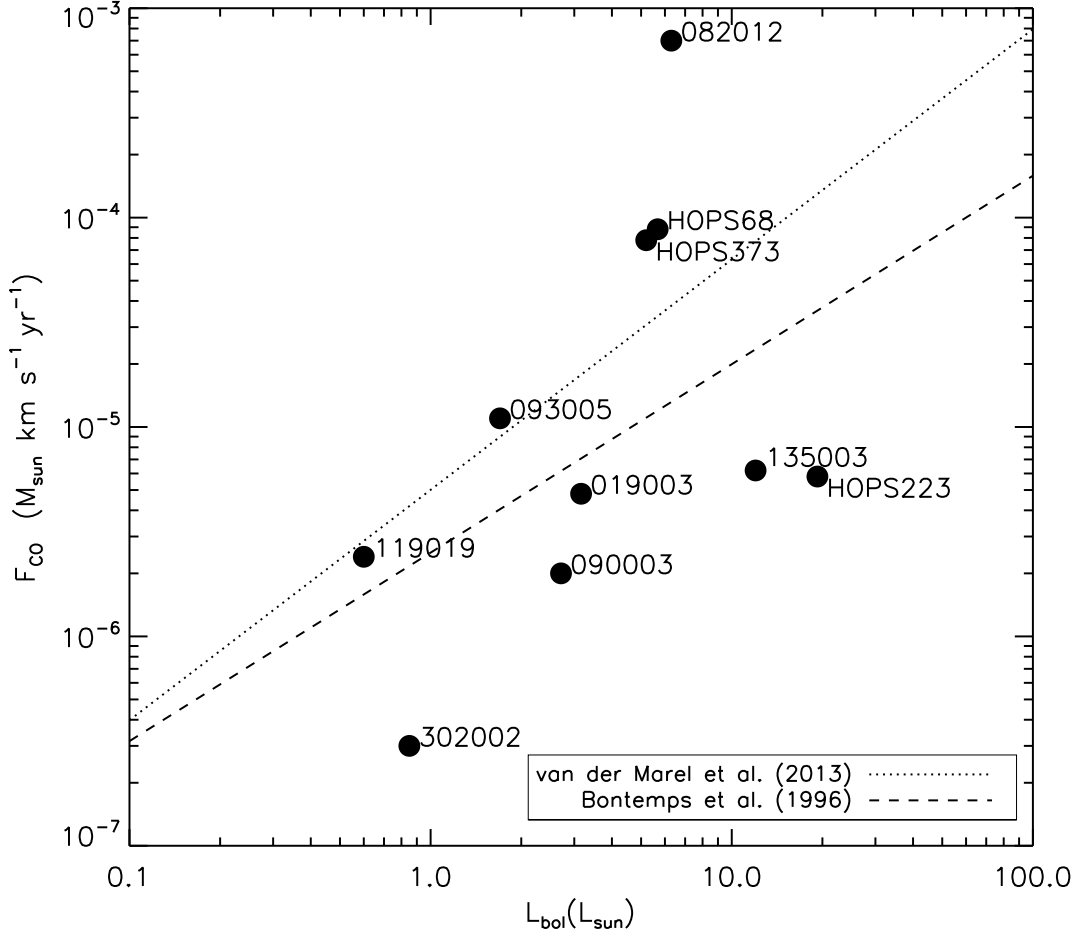


Fig. 11.— Measured outflow forces ( $F_{CO}$ ) versus  $L_{bol}$  for all sources with detected outflows. There is no clear relationship between these two source properties in our data; however, there is a general tendency of high luminosity sources having greater outflow forces. We plot the relationships that have been found in the literature for larger samples of objects from van der Marel et al. (2013) (dotted line) and Bontemps et al. (1996) (dashed line). The literature relationships utilized single-dish data, while our data are interferometric; thus, missing flux could cause  $F_{CO}$  to be systematically underestimated. Furthermore, the Class 0 sources in the literature have  $F_{CO}$  and  $L_{bol}$  values that are above the Bontemps et al. (1996) relation and the plotted relationships are principally fit to the Class I protostars.

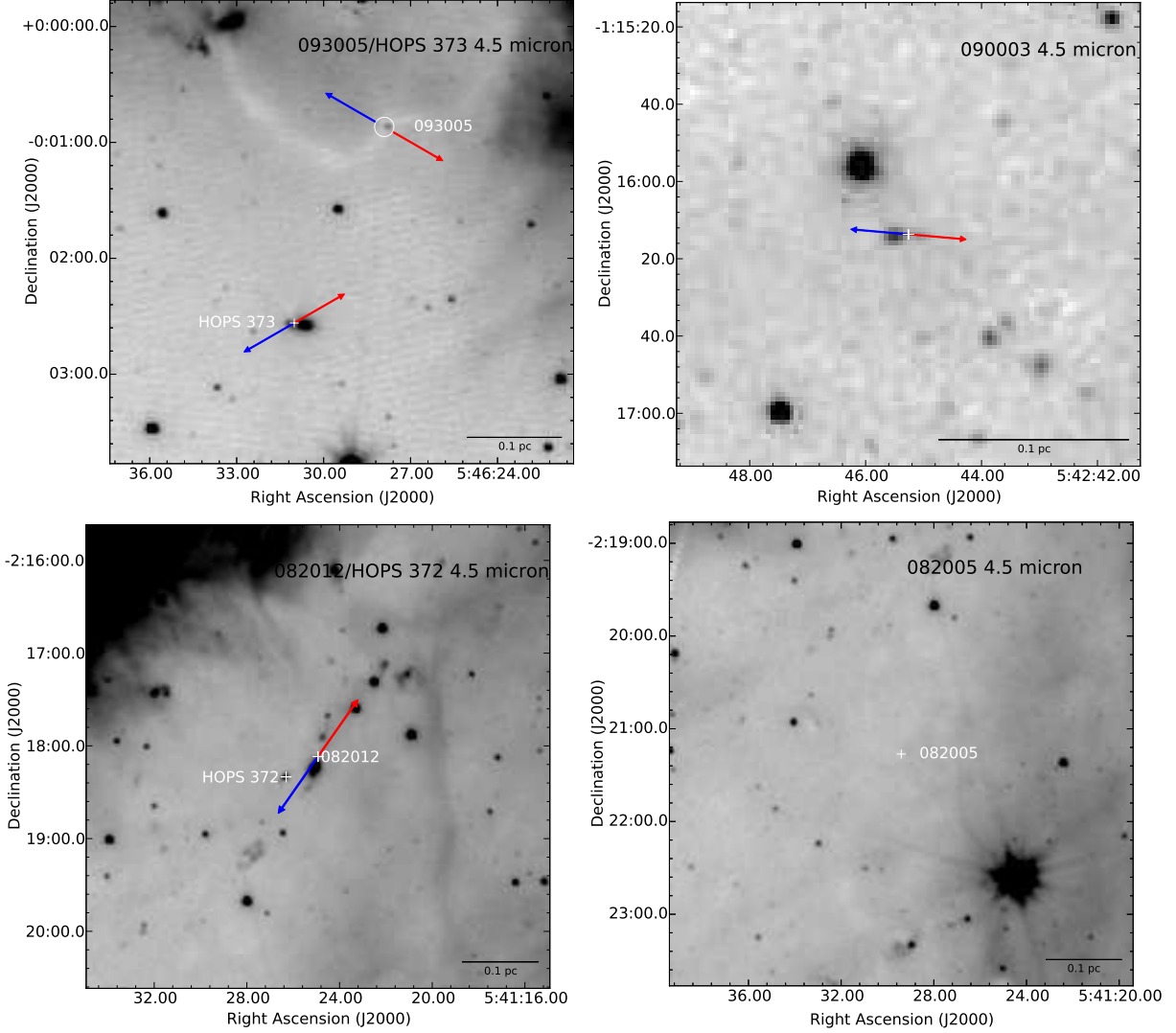


Fig. 12a.— *Spitzer* 4.5  $\mu\text{m}$  images of the PBRs sample also having CO ( $J = 1 \rightarrow 0$ ) observations. This particular *Spitzer* band has a bright  $\text{H}_2$  feature commonly associated with shock-excited outflow emission but is also sensitive to scattered light in the outflow cavities. The protostars positions are marked with either white crosses or small circles and the outflow position angles are denoted by the red and blueshifted arrows. The PBRs 093005, 090003, HOPS 373, and 302002 have compact 4.5  $\mu\text{m}$  emission near the location of the protostars and no extended  $\text{H}_2$  knots. The PBRs 061012, HOPS 223, 082012, and 119019 have indications of  $\text{H}_2$  emission extended  $\gtrsim 0.1$  pc from the protostars. Moreover, in the 061012 field the protostars HOPS 221 shows another apparent east-west outflow. The protostars 091015, 091016, 097002, and 082005 do not show evidence of any emission shortward of 70  $\mu\text{m}$ . The source near the location of 097002 is another young star and not the PBRs (ST13).

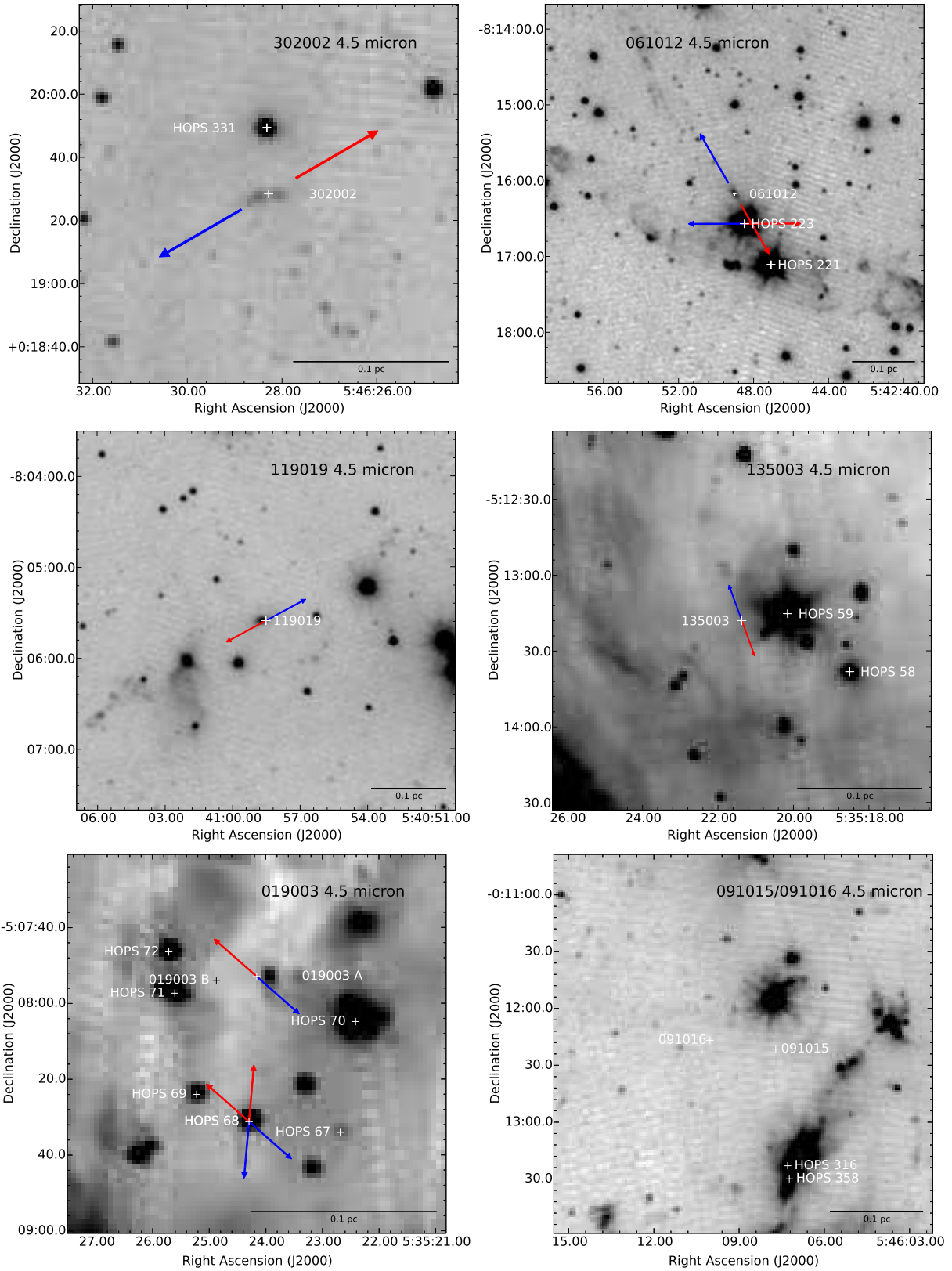


Fig. 12b.—

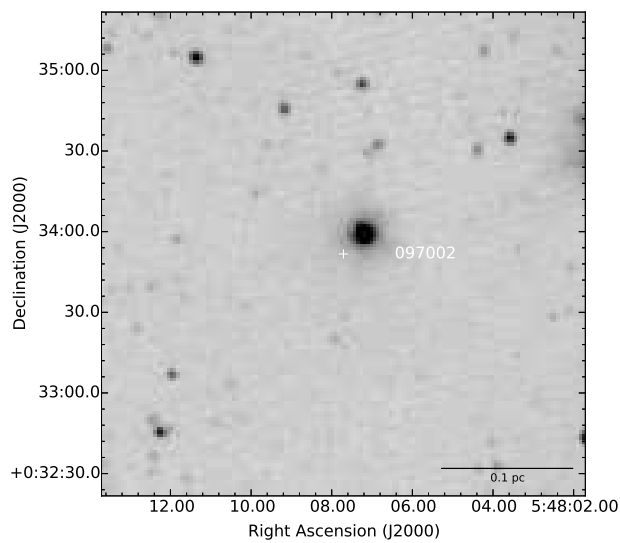


Fig. 12c.—

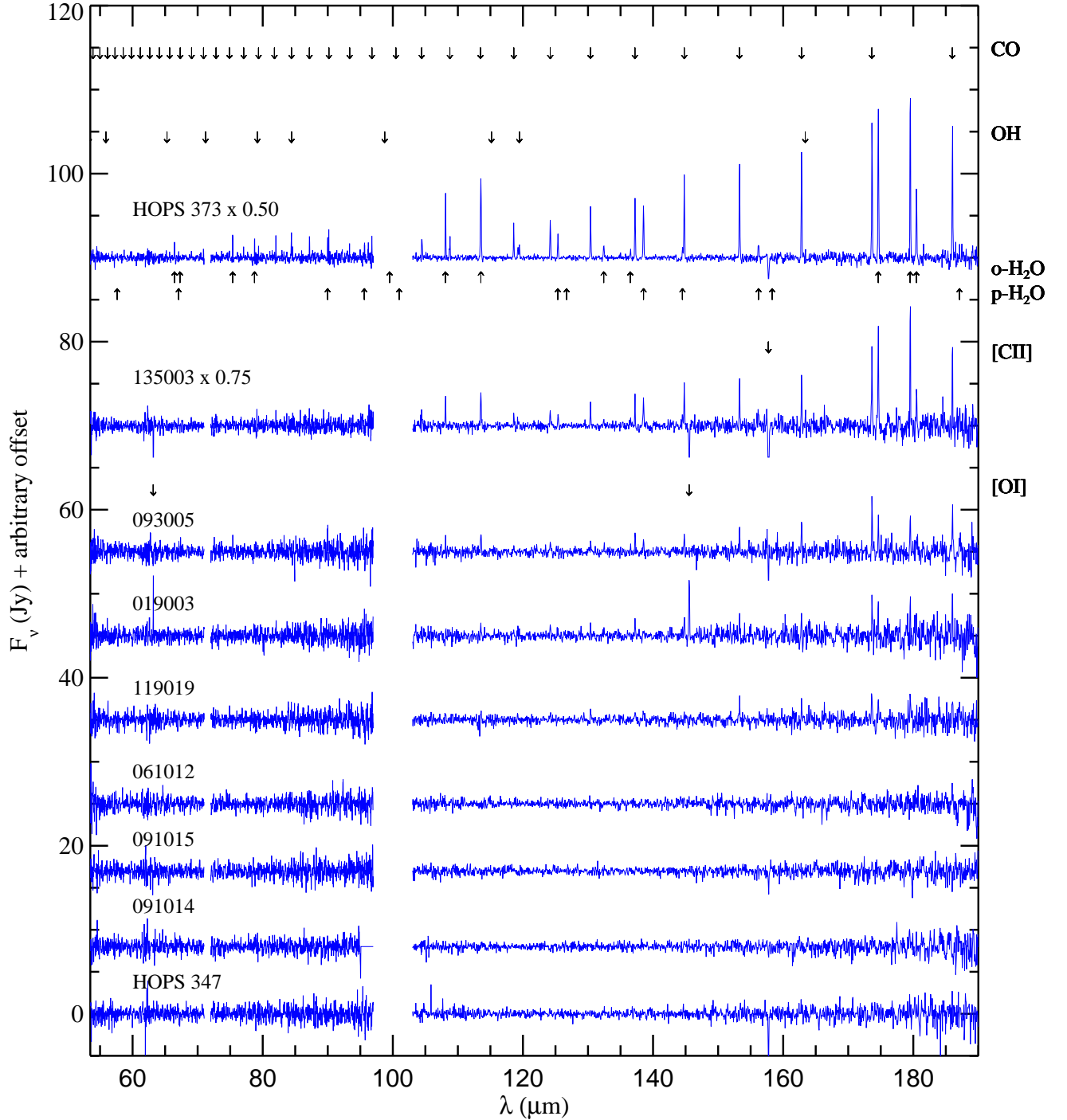


Fig. 13.— Continuum subtracted PACS Spectra for the observed sample; the sources are plotted in descending order of line brightness. The wavelengths of common spectral lines are marked with arrows with labels located to the right of the plot. Negative features are not absorption, but reflect line contamination in the off position. Only [OI] (63  $\mu\text{m}$  and 143  $\mu\text{m}$ ) and [CII] were found to be contaminated by the off positions for some sources.

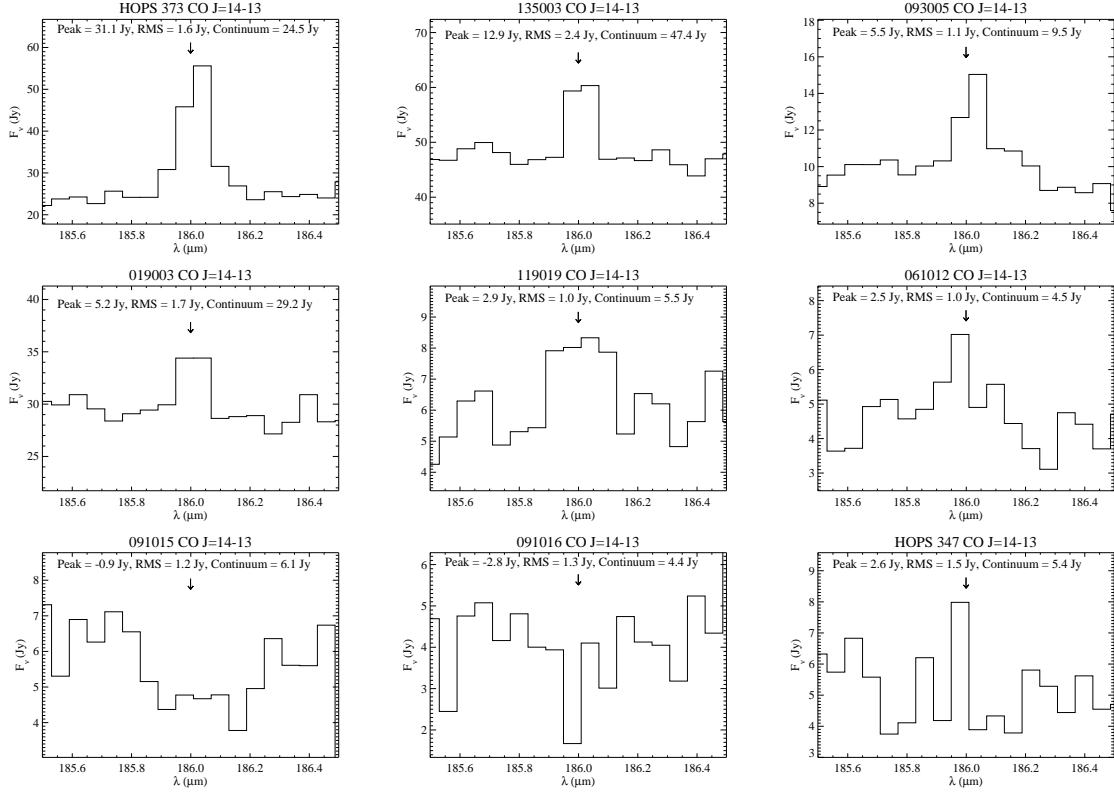


Fig. 14.— PACS spectra centered on the CO ( $J = 14 \rightarrow 13$ ) transition without continuum subtraction. The downward pointing arrow marks the wavelength of CO ( $J = 14 \rightarrow 13$ ). We also note the peak line flux density, rms of the continuum, and continuum level in each plot; the peak line flux density is relative to the continuum level. PBRs 119019 only has a  $2.9\sigma$  detection of the CO ( $J = 14 \rightarrow 13$ ), but other CO transitions are detected with higher significance, thus we regard this as a robust detection. On the other hand the PBRs 061012 has only a tentative ( $2.5\sigma$ ) detection of CO ( $J = 14 \rightarrow 13$ ) and no other CO transitions detected; 091015 and 091016 do not have detections. HOPS 347 has a peak at the expected wavelength of CO ( $J = 14 \rightarrow 13$ ) but it is not significant given the noise around the line. The peak line flux density, RMS, and continuum level are denoted in each plot.

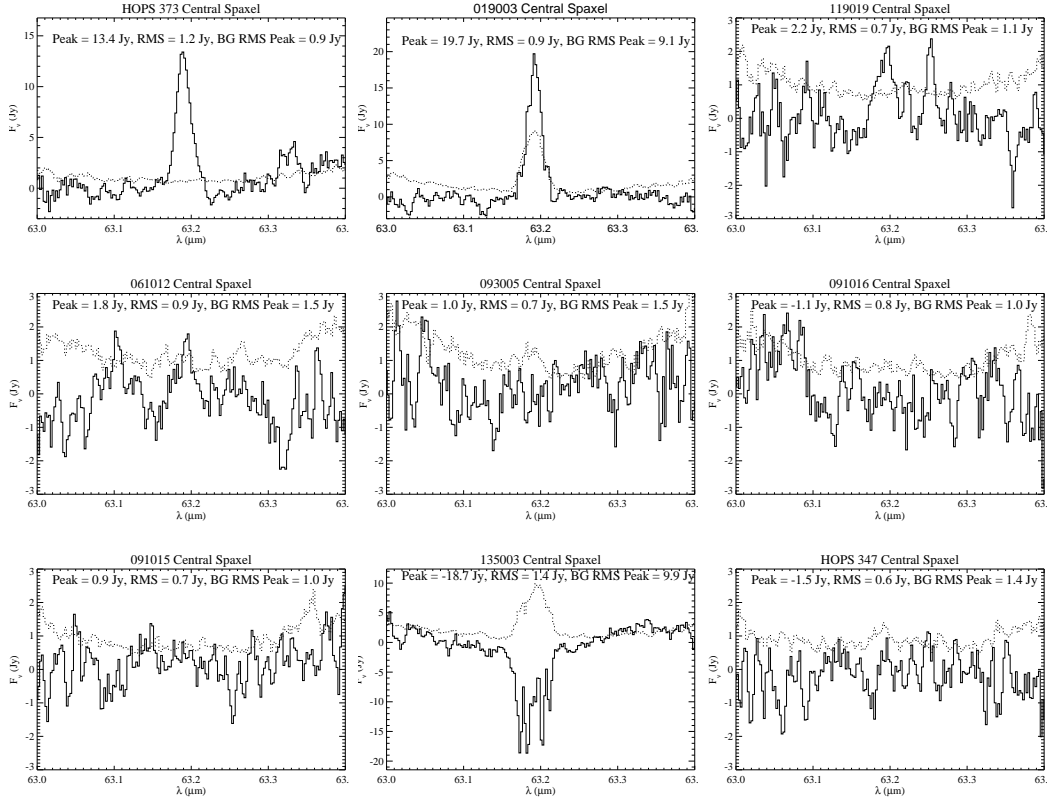


Fig. 15.— PACS spectra around the [OI]  $63.18 \mu\text{m}$  transition. The solid-line is the foreground/background subtracted spectrum. The foreground/background is measured from the edge spaxels and the fine dashed line is the standard deviation of the foreground/background spectrum. This is a good representation of the noise level in the spectral band since the [OI] variations will dominate the noise. Only HOPS 373 has a convincing detection in the [OI] line, the detection of 019003 is tentative ( $2.2\sigma$ ) given the large variations in the foreground/background spectrum. There are features at the expected wavelength of [OI] toward 061012 and 119019, but there are other features that have the same level of peak intensity that do not correspond to an expected spectral line. The foreground/background [OI] near 135003 is highly variable, resulting in the negative spectrum. The peak line flux density, spectrum RMS, and the RMS of the background (BG RMS Peak) emission at the wavelength of the [OI] line are noted in each panel.

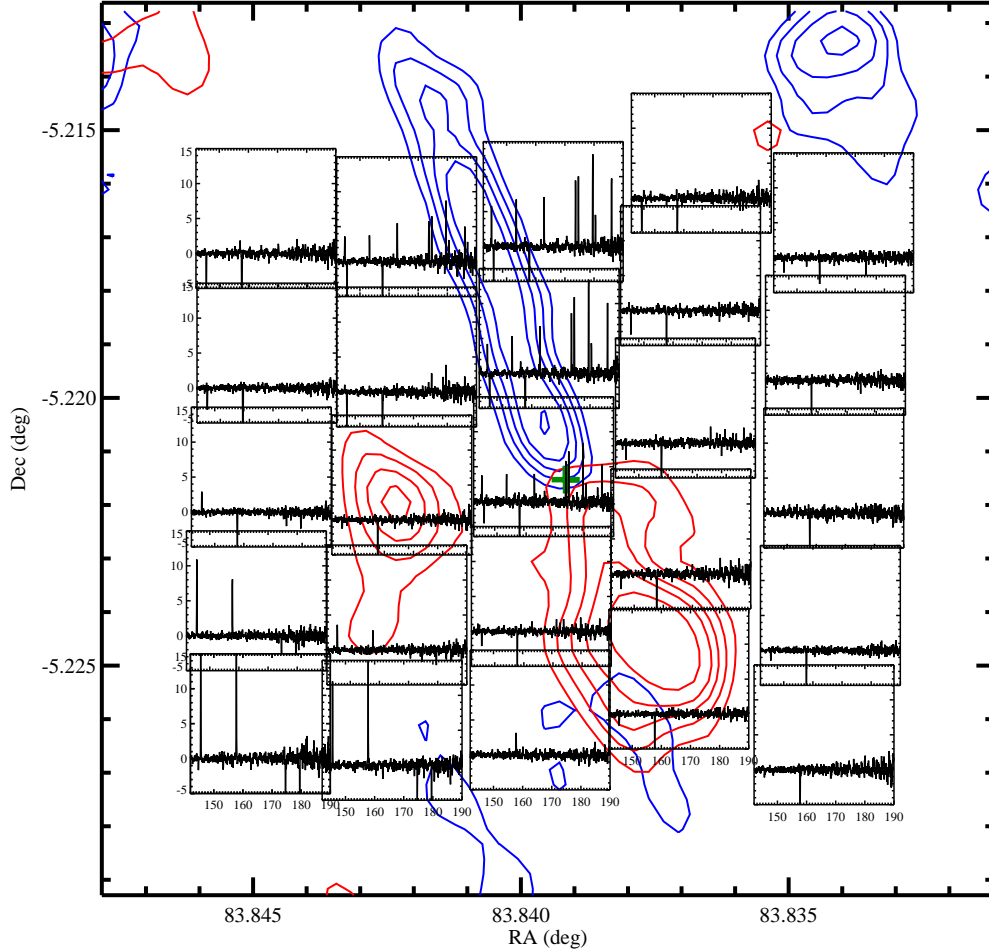


Fig. 16a.— PACS Spectrometer footprint observed toward PBRs 135005 and overlaid on the CO ( $J = 1 \rightarrow 0$ ) contours from Figure 5, plotting the positive contours only. The plots of the two long wavelength channels of the spectrometer show remarkable correspondence between the blue-shifted (north) side of the CO outflow and high- $J$  water and CO line emission. The wavelength range from  $140 \mu\text{m}$  to  $190 \mu\text{m}$  is shown in (a) and  $100 \mu\text{m}$  to  $140 \mu\text{m}$  is shown in (b). There is an apparent lack of similar high- $J$  CO and water emission on the red-shifted side of the outflow (south); however, maps of the far-infrared and submillimeter continuum show that there is extended cold dust emission north of 135003 but not south. Therefore, the blue-shifted outflow is likely impacting ambient material causing shocks, while the red-shifted outflow is being driven into a less dense medium. The green cross in the central spaxel marks the location of the 2.9 mm continuum source, where the red and blue-shifted contours meet.

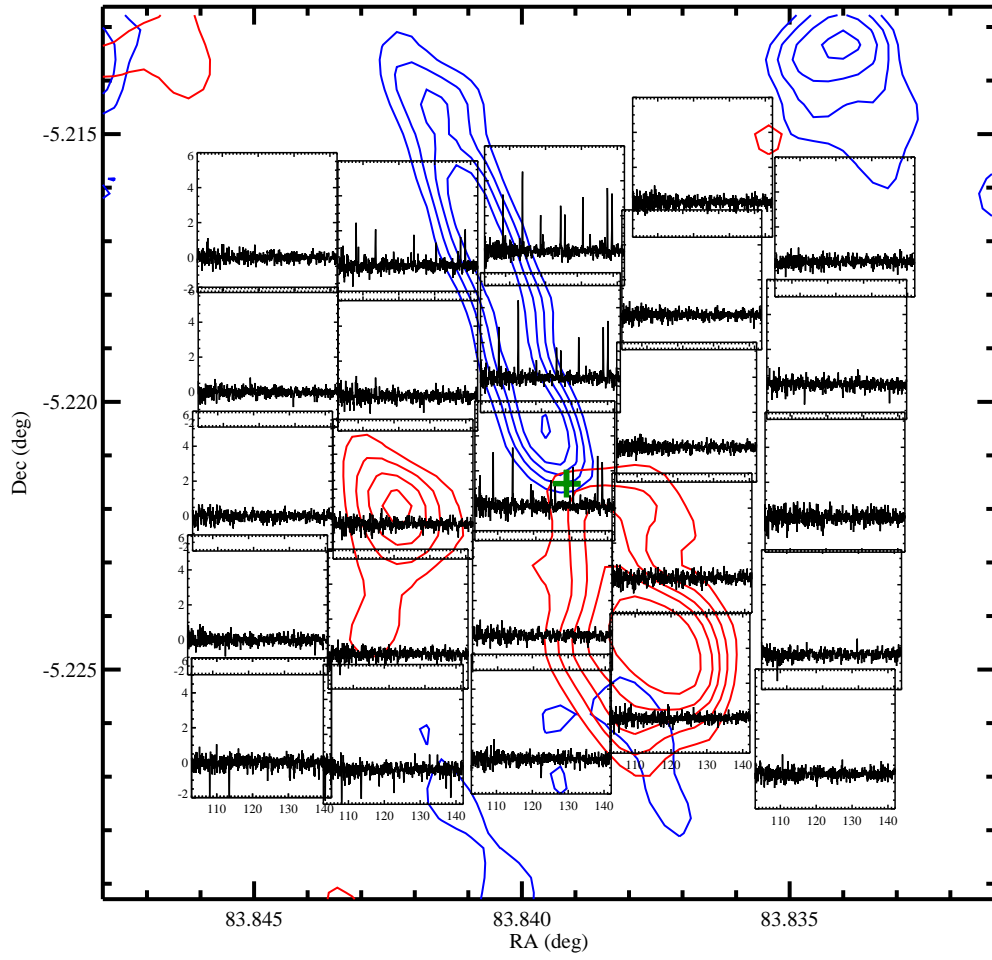


Fig. 16b.—

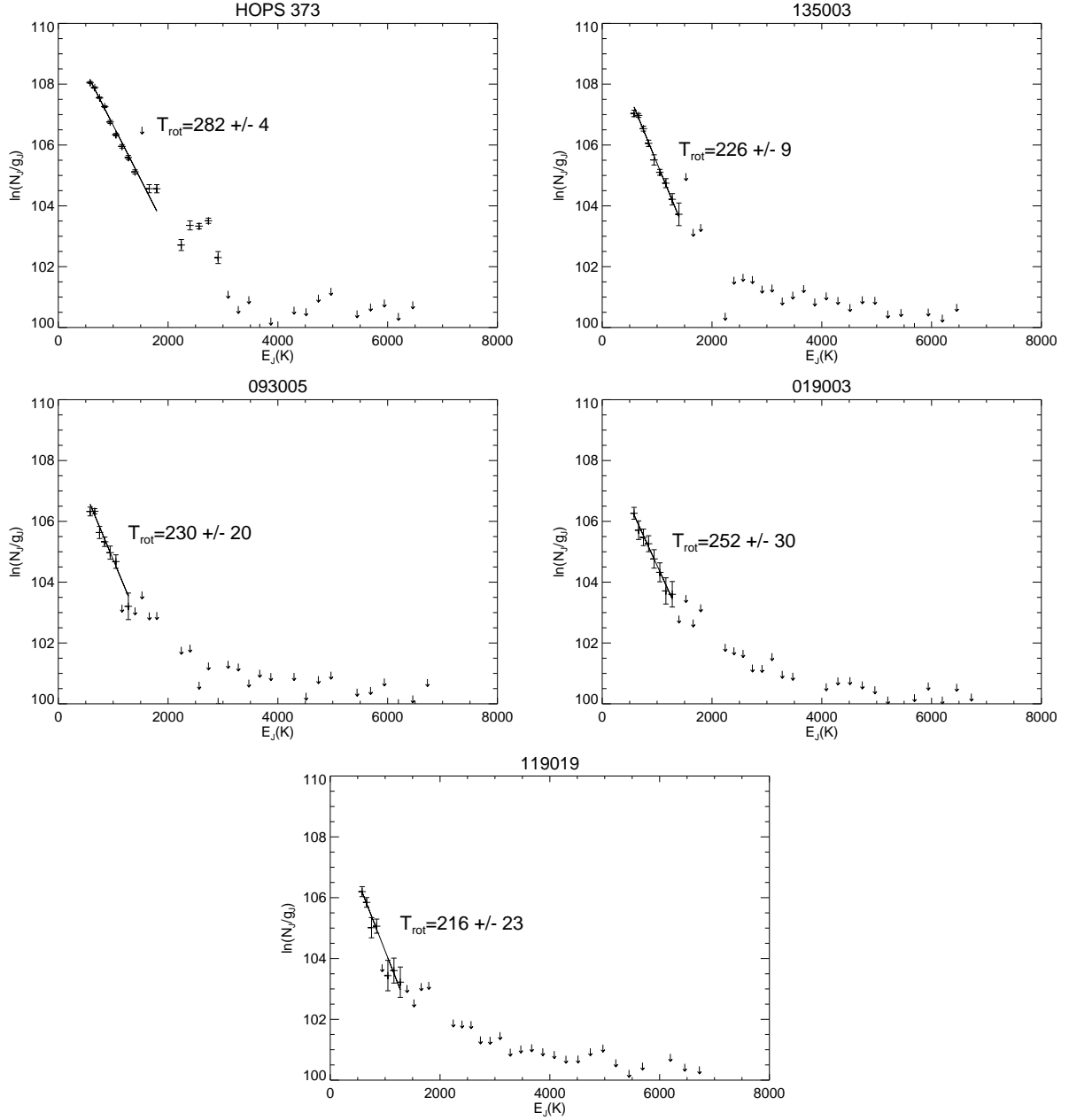


Fig. 17.— Rotation diagrams of PACS CO emission, assuming optically thin emission. The quantity plotted on the y-axis is the natural logarithm of the total number of CO molecules in the  $J$ th state divided by the degeneracy of that state.

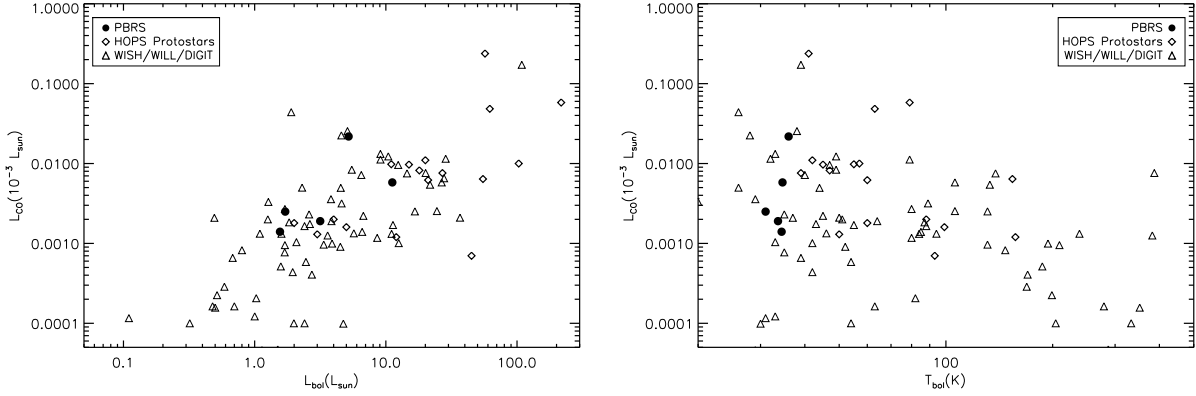


Fig. 18.— CO luminosity versus  $L_{bol}$  (left) and  $T_{bol}$  (right) for the PBRS, and WISH/WILL/DIGIT/HOPS samples. The CO luminosity for the PBRS and HOPS sources is a summation of all detected CO lines in the PACS spectral range for the PBRS, and WISH/WILL/DIGIT/HOPS samples. The WISH and WILL CO luminosities are calculated by extrapolation of the CO ladder given that not all CO lines were observed.

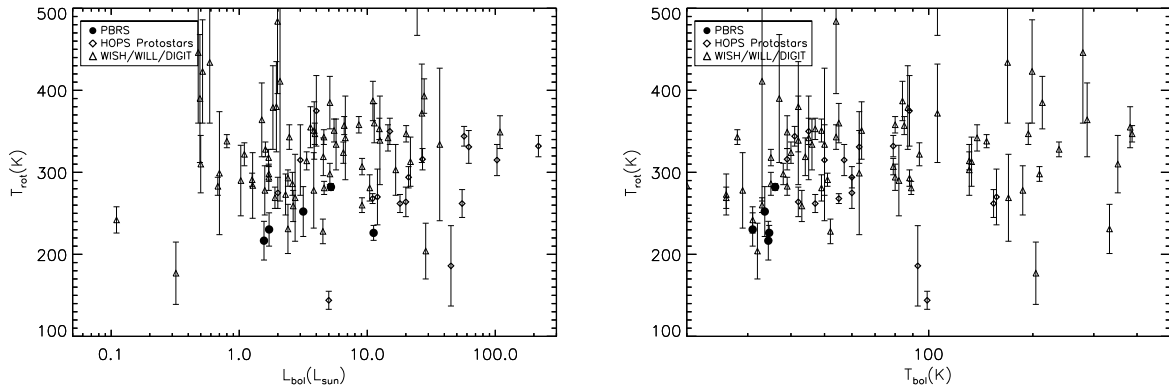


Fig. 19.— CO rotation temperatures ( $T_{rot}$ ) of the PBRS relative to the WISH/WILL/DIGIT/HOPS samples. The  $T_{rot}$  values for the PBRS are among the lowest measured for the luminosity range sampled and are lower than most protostars with similar  $T_{bol}$  measurements. The source with the lowest  $L_{bol}$  is IRAM 04191 from the DIGIT sample (Green et al. 2013).

Table 1. CARMA CO ( $J = 1 \rightarrow 0$ ) Observations

Source	HOPS #	Configuration(s)	Beam (")	Line RMS (Jy beam <sup>-1</sup> chan <sup>-1</sup> )
097002	404	D	$6.8 \times 5.0$	0.1
HOPS 373 <sup>a</sup>	373	D+C	$3.3 \times 3.0$	0.15
302002	407	D	$4.9 \times 3.7$	0.13
093005	403	D+C	$2.9 \times 2.7$	0.11
091016	402	D+C	$2.3 \times 2.2$	0.1
091015	401	D+C	$2.3 \times 2.2$	0.1
061012/HOPS 223	397	D	$5.4 \times 4.1$	0.19
090003	400	D+C	$3.2 \times 2.9$	0.11
082005	398	D+C	$3.1 \times 2.9$	0.1
082012/HOPS 372 <sup>a</sup>	399	D+C	$4.5 \times 4.1$	0.15
119019	405	D	$6.3 \times 3.4$	0.12
019003 A/HOPS 68	394	D	$5.4 \times 3.7$	0.15
135003	409	D	$5.4 \times 3.7$	0.12

Note. — The RMS values given are for  $0.5 \text{ km s}^{-1}$  channel widths.

<sup>a</sup>UV tapering applied, increasing the beam size and sensitivity to the extended outflow structures.

Table 2. *Herschel* Observation Log

Source	Date (UT)	Obs. ID
PACS Full Range Scans		
135003	2012-09-14	1342250990, 1342250991
HOPS 347	2012-09-24	1342251350, 1342251351
093005	2012-09-24	1342251352, 1342251353
019014	2012-09-24	1342251355, 1342251356
019015	2012-09-25	1342251357, 1342251358
019003	2012-09-25	1342251359, 1342251360
119019	2012-09-25	1342251361, 1342251361
HOPS 373	2012-10-02	1342252083, 1342252084
061012	2012-10-02	1342252085, 1342252086
[OI] 63 $\mu\text{m}$ Unchopped Line Spectroscopy		
019003	2012-08-14	1342249505
HOPS 347	2012-09-12	1342250913
093005	2012-09-12	1342250914
091015	2012-09-12	1342250988
091014	2012-09-14	1342250915
061012	2012-09-14	1342250915
119019	2012-09-14	1342250992
135003	2012-09-14	1342250993
HOPS 373	2012-09-24	1342251354

Table 3. PBRs Observational Summary

Source	HOPS ID	RA (J2000)	Dec (J2000)	CARMA Data	<i>Herschel</i> PACS Spectra
HOPS 354	354	05:54:24.1	01:44:20.2	...	...
097002	404	05:48:07.71	00:33:51.7	x	...
HOPS 359	359	05:47:24.8	00:20:58.2	...	...
HOPS 341	341	05:47:00.9	00:26:20.8	...	...
HOPS 373	373	05:46:30.99	-00:02:33.9	x	x
302002	407	05:46:28.28	00:19:28.1	x	...
093005	403	05:46:27.90	-00:00:52.1	x	x
091016	402	05:46:10.01	-00:12:17.3	x	x
091015	401	05:46:07.72	-00:12:21.3	x	x
HOPS 358	358	05:46:07.2	-00:13:30.9	...	...
061012	397	05:42:49.03	-08:16:11.8	x	x
090003	400	05:42:45.26	-01:16:13.9	x	...
082005	398	05:41:29.40	-02:21:16.5	x	...
HOPS 372	372	05:41:26.34	-02:18:21.6	x	...
082012	399	05:41:24.92	-02:18:07.0	x	...
119019	405	05:40:58.56	-08:05:35.0	x	x
HOPS 169	169	05:36:36.0	-06:38:54.0	...	...
019003 A	394	05:35:24.23	-05:07:53.9	x	x
135003	409	05:35:21.40	-05:13:17.5	x	x

Note. — Summary of observational follow-up data for the PBRs. All PBRs have imaging data from *Spitzer* and *Herschel*. The PBRs 135003 was not included in ST13 because its full width at half-maximum was slightly larger than the cutoff value adopted by ST13 to filter out extended structures that were not protostellar sources. However, further examination revealed that it was a robustly detected PBRs and it was included in subsequent follow-up observations.



Table 4. CO ( $J = 1 \rightarrow 0$ ) Outflow Properties

Source	PA ( $^{\circ}$ )	Length (AU)	$\delta v_{max}$ ( $\text{km s}^{-1}$ )	Blue Lobe			Red Lobe			Total			Force ( $\text{M}_{\odot} \text{ km s}^{-1} \text{ yr}^{-1}$ )	$T_{d,gr}$ (yr)
				Mass ( $\text{M}_{\odot}$ )	Momentum ( $\text{M}_{\odot} \text{ km s}^{-1}$ )	Energy ( $10^{40} \text{ erg}$ )	Mass ( $\text{M}_{\odot}$ )	Momentum ( $\text{M}_{\odot} \text{ km s}^{-1}$ )	Energy ( $10^{40} \text{ erg}$ )	Mass ( $\text{M}_{\odot}$ )	Momentum ( $\text{M}_{\odot} \text{ km s}^{-1}$ )	Energy ( $10^{40} \text{ erg}$ )		
P2013 min <sup>a</sup>	...	5000	...	...	...	...	...	...	...	...	...	...	...	...
P2013 max	...	90000	...	...	...	...	...	...	...	...	...	...	...	...
AS2006 min <sup>b</sup>	...	...	...	...	...	...	...	...	...	...	...	...	...	...
AS2006 max	...	...	...	...	...	...	...	...	...	...	...	...	...	...
HOPS 373	123	$\geq 31000$	18	0.03	0.14	760	0.13	0.5	2100	0.16	0.64	2860	$78.0 \times 10^{-6}$	8200
082012 <sup>c</sup>	151	$\geq 42000$	70	0.08	0.7	11000	0.08	1.2	27000	0.16	2.0	38000	$700 \times 10^{-6}$	2900
093005	238	4200	22	0.001	0.005	36.0	0.0008	0.005	34.0	0.0018	0.01	70.0	$11.0 \times 10^{-6}$	900
090003	86	7300	14	0.001	0.004	12.0	0.0004	0.001	3.6	0.0005	0.005	15.6	$2.0 \times 10^{-6}$	2500
135003	21	$\geq 42000$	40	0.003	0.015	87.0	0.003	0.016	91.0	0.006	0.031	178.0	$6.2 \times 10^{-6}$	5000
119019	114	$\geq 42000$	8	0.02	0.04	61.0	0.01	0.02	29.0	0.03	0.06	90.0	$2.4 \times 10^{-6}$	25000
302002	122	$\geq 31000$	4	0.004	0.007	14.8	0.002	0.002	1.9	0.006	0.01	16.7	$0.3 \times 10^{-6}$	37000
019003 A	230	$\geq 21000$	16	0.003	0.02	121	0.002	0.01	61.0	0.005	0.03	82	$4.8 \times 10^{-6}$	6300
HOPS 68 <sup>c</sup>	230, 166	$\geq 15000$	70	0.01	0.06	380	0.006	0.03	199	0.04	0.09	579	$88.0 \times 10^{-6}$	1020
HOPS 223	90	$\geq 31000$	20	0.001	0.03	120	0.005	0.02	90	0.006	0.05	210	$5.8 \times 10^{-6}$	8600
061012	58	$\geq 4200$	$\sim 15$											
HOPS 372 <sup>d</sup>	141	$\geq 10000$	$\sim 10$											

Note. — These quantities are derived following the analysis in Plunkett et al. (2013) which is based on Bally et al. (1999). These quantities are at best lower limits given that substantial emission is resolved-out near line center and the outflows were not detected in our  $^{13}\text{CO}$  data, the inclusion of  $^{13}\text{CO}$  would enable us to more accurately calculate the optical depth of  $^{12}\text{CO}$ . The last column,  $T_{d,gr}$  is derived from dividing the outflow length by  $\delta v_{max}$ .

<sup>a</sup>Range of parameters listed for all outflows identified in Plunkett et al. (2013).

<sup>b</sup>Range of parameters listed for the Class 0 outflows listed in Arce & Sargent (2006).

<sup>c</sup>Source likely has two blended outflows, properties listed are for both outflows combined.

<sup>d</sup>Outflow extent, position angle, and velocity width uncertain due to blending with another outflow.

Table 5. PBRS Summary Table

Source	HOPS ID	$M_{env}$	$L_{bol}$ ( $M_{\odot}$ )	$T_{bol}$ ( $L_{\odot}$ )	Visibilities (K)	CO ( $J = 1 \rightarrow 0$ )	Inclination outflow	4.5 $\mu\text{m}$	PACS lines	[OI]
097002	404	$2.8 \pm 0.3$	1.14	33.4	flat	no	...	no	...	...
HOPS 373	373	$3.1 \pm 0.4$	5.2	36.0	decline	ext	$\sim 50^{\circ}$	comp	yes	yes
302002	407	$2.9 \pm 0.3$	0.85	28.6	decline	ext (low S/N)	$\sim 80^{\circ}$	comp	...	...
093005	403	$5.4 \pm 0.6$	1.7	30.8	flat	comp	$\sim 30^{\circ}$	comp	yes	no
091016	402	$2.8 \pm 0.3$	0.65	29.1	flat	no	...	no	no	no
091015	401	$1.9 \pm 0.3$	0.81	30.9	flat	no	...	no	no	no
061012	397	$1.0 \pm 0.2$	0.75	32.1	decline?	comp (low S/N)	...	ext	marginal	no
090003	400	$7.0 \pm 0.7$	2.71	36.0	flat	comp	$\sim 30^{\circ}$	comp	...	...
082005	398	$2.0 \pm 0.3$	1.02	29.3	flat	no	...	no	...	...
HOPS 372	372	$2.2 \pm 0.4$	4.9	36.9	decline?	ext (blend)	...	ext	...	...
082012	399	$9.4 \pm 1.0$	6.3	32.2	decline	ext	$\sim 50^{\circ}$	ext	...	...
119019	405	$0.6 \pm 0.1$	1.56	34.4	decline	ext	$\sim 90^{\circ}$	ext	yes	no
019003 A	394	$2.4 \pm 0.3$	3.16	33.6	decline	ext	$\sim 30^{\circ}$	comp	yes	no
135003	409	$3.0 \pm 0.4$	12.0	30.0	decline	ext	$\sim 50^{\circ}$	ext	yes	no

Note. — Summary table for PBRS properties.  $L_{bol}$  and  $T_{bol}$  are from ST13 and Tobin et al. (2015); the visibility amplitude profiles, envelope masses, and 2.9 mm flux densities are from Tobin et al. (2015). With regard to the CO outflows, ‘ext’ refers to extended emission, while ‘comp’ refers to compact emission; compact being less than  $12''$  (5000 AU) in extent. Also, the tentative CO outflows are denoted with either ‘low S/N’ or ‘blend’ in the table. The 4.5  $\mu\text{m}$  emission is used to trace shocked  $\text{H}_2$  emission in the outflows, ‘comp’ means there is emission located within  $10''$  and a ‘ext’ means that there are apparent  $\text{H}_2$  knots more than  $10''$  from the source but in the outflow direction.

Table 6. Far-Infrared Spectral Properties

Source	HOPS ID	L(CO) ( $10^{-3} L_{\odot}$ )	CO $T_{rot}$ (K)	L([OI]) ( $10^{-3} L_{\odot}$ )	$\dot{M}_{wind}$ ([OI]) ( $M_{\odot} \text{ yr}^{-1}$ )
HOPS 373	373	$21.8 \pm 0.3$	$282 \pm 4$	$1.3 \pm 0.05$	$1.1 \times 10^{-7}$
093005	403	$2.5 \pm 0.2$	$230 \pm 20$	$< 0.1$	$< 2.8 \times 10^{-9}$
091016	402	$< 0.5$	...	$< 0.11$	$< 3.1 \times 10^{-9}$
091015	401	$< 0.5$	...	$< 0.15$	$< 4.7 \times 10^{-9}$
061012	397	$0.2 \pm 0.1$	...	$< 0.12$	$< 9.5 \times 10^{-9}$
119019	405	$1.4 \pm 0.2$	$217 \pm 24$	$< 0.15$	$< 1.6 \times 10^{-8}$
019003 A	394	$1.9 \pm 0.25$	$252 \pm 30$	$< 1.6$	$< 1.4 \times 10^{-7}$
135003	409	$5.8 \pm 0.25$	$226 \pm 9$	$< 3.5$	$< 9.5 \times 10^{-8}$
HOPS 347	347	$< 0.5$	...	$< 0.13$	$< 3.6 \times 10^{-9}$

Note. — The far-infrared CO luminosities are calculated by summing all the detected line flux densities and converted to luminosity, assuming a distance of 420 pc. The L([OI]) only considers emission from the  $63.18 \mu\text{m}$  line and the  $\dot{M}_{wind}$  ([OI]) is calculated by multiplying L([OI]) by  $8.1 \times 10^{-5} M_{\odot} \text{ yr}^{-1} L_{\odot}^{-1}$  (Hollenbach 1985). The upper limits given for the line luminosities are  $3\sigma$  upper limits.

Table 7. PACS Line Ratios

Source	CO 16-15 /CO 21-20	CO 17-16 /CO 22-21	CO 16-15 /CO 17-16	CO 21-20 /CO 22-21	H <sub>2</sub> O 2 <sub>12</sub> -1 <sub>01</sub> /H <sub>2</sub> O 4 <sub>04</sub> -3 <sub>13</sub>	H <sub>2</sub> O 4 <sub>04</sub> -3 <sub>13</sub> /CO 16-15	H <sub>2</sub> O 4 <sub>04</sub> -3 <sub>13</sub> /CO 21-20	OH 84 /OH 79	CO 16-15 /OH 84	H <sub>2</sub> O 4 <sub>04</sub> -3 <sub>13</sub> /OH 84
WISH/WILL	1.2-2.5	-	-	-	1.3-6.3	0.1-0.5	0.2-0.9	1.1-2.4	0.4-2.8	0.08-0.9
019003	3.26±1.63	15.36±13.51	0.35±0.13	1.67±1.57	1.29±0.63	0.30±0.14	0.99±0.57	...	...	...
093005	5.69±2.72	11.60±9.18	0.39±0.10	0.80±0.71	2.43±2.64	0.12±0.13	0.69±0.79	...	...	...
119019	3.01±1.80	...	0.27±0.11	...	...	...	...	...	...	...
135003	5.12±1.04	8.89±3.43	0.47±0.06	0.81±0.34	4.29±1.09	0.17±0.04	0.85±0.26	...	...	...
HOPS 373	3.59±0.26	7.36±0.56	0.39±0.02	0.79±0.08	3.11±0.31	0.16±0.02	0.59±0.07	3.27±1.20	3.34±0.51	0.54±0.10